Organoid culture promotes dedifferentiation of mouse myoblasts into stem cells capable of complete muscle regeneration

Feodor D. Price [1,2,3,4] ✉, Mark N. Matyas[1,2], Andrew R. Gehrke[5], William Chen [1,2], Erica A. Wolin[1,2], Kristina M. Holton[1,2,3], Rebecca M. Gibbs[1,2], Alice Lee[1,2], Pooja S. Singu [1], Jeffrey S. Sakakeeny[1], James M. Poteracki [1], Kelsey Goune [1], Isabella T. Pfeiffer [1], Sarah A. Boswell [4], Peter K. Sorger [4], Mansi Srivastava[5], Kathleen Lindahl Pfaff[1,2], Emanuela Gussoni [6], Sean M. Buchanan[1,2] & Lee L. Rubin [1,2,3] ✉

Experimental cell therapies for skeletal muscle conditions have shown little success, primarily because they use committed myogenic progenitors rather than true muscle stem cells, known as satellite cells. Here we present a method to generate in vitro-derived satellite cells (idSCs) from skeletal muscle tissue. When transplanted in small numbers into mouse muscle, mouse idSCs fuse into myofibers, repopulate the satellite cell niche, self-renew, support multiple rounds of muscle regeneration and improve force production on par with freshly isolated satellite cells in damaged skeletal muscle. We compared the epigenomic and transcriptional signatures between idSCs, myoblasts and satellite cells and used these signatures to identify core signaling pathways and genes that confer idSC functionality. Finally, from human muscle biopsies, we successfully generated satellite cell-like cells in vitro. After further development, idSCs may provide a scalable source of cells for the treatment of genetic muscle disorders, trauma-induced muscle damage and age-related muscle weakness.

Satellite cells, the canonical muscle stem cells, are responsible for postnatal muscle growth and regeneration. They exist in a quiescent state, located in a niche between the basal lamina and muscle sarcolemma[1–5]. During muscle regeneration, these cells activate, divide asymmetrically to self-renew or form a proliferative population of committed progenitors called myoblasts. These myoblasts differentiate and fuse to form myotubes, the functional component of skeletal muscle[6–8]. Without satellite cells, skeletal muscle regeneration is completely abolished[2,9,10]. After muscle development or regeneration, some satellite cells return to quiescence and repopulate the niche in preparation for future rounds of regeneration[8].

Many have hypothesized that transplanted satellite cells could treat muscle diseases and traumatic muscle injuries[8,11]. However, satellite cells are rare in skeletal muscle, so large quantities cannot be obtained from postnatal muscle tissue. Furthermore, although several decades of research have provided a deep understanding of the functional properties of satellite cells, it is not known yet how to effectively increase their numbers in culture while maintaining their stem cell

characteristics, particularly preserving their ability to repopulate the niche[12,13]. In conventional tissue culture conditions, satellite cells enter the cell cycle and become myoblasts[8]. However, satellite cells and myoblasts have key differences. Although both can produce muscle fibers, after transplant, satellite cells are up to 1,000 times more efficient at this process[7,12,14]. Only satellite cells can repopulate the stem cell niche, self-renew and sustain muscle regeneration over the lifetime of an organism[6,7,12,14]. These critical differences between satellite cells and myoblasts underscore the need to generate therapeutically relevant quantities of satellite cells in vitro.

Culturing cells in three dimensions can recreate stem cell niche conditions for several tissues, enabling adult stem cell expansion while retaining their capacity to differentiate and mature[15–18]. Evidence shows that adult progenitor cells in the tooth, liver, gut and pancreas dedifferentiate into a stem cell-like state in vivo and, in some cases, in three-dimensional (3D) cultures[19–21]. We studied the effect of 3D culture on proliferating adult myoblasts. Myoblasts can generate skeletal muscle organoids (SkMOs) containing cells resembling satellite cells, termed in vitro-derived satellite cells (idSCs). Upon transplantation into damaged or diseased muscle, idSCs regenerate muscle similarly to satellite cells. Although idSCs share key pathways known to regulate quiescence and myogenic commitment, they are transcriptionally and epigenomically distinct, raising several interesting questions regarding the relationship between in vitro and in vivo cellular identities.

Results

SkMOs contain satellite-like cells

Satellite cells express *Pax7*, an essential transcription factor (TF) for satellite cell maintenance and commitment[2,22]. During skeletal muscle regeneration, myoblasts maintain *Pax7* expression but activate *MyoD*, a TF involved in myogenic commitment and differentiation[23,24]. *MyoD* expression, coupled with the downregulation of *Pax7*, commits cells to differentiation, resulting in the loss of stem cell potential[12]. To investigate whether myoblasts (Pax7+MyoD+) can reduce the expression of MyoD and dedifferentiate back to a satellite cell-like state (Pax7+MyoD−), we seeded myoblasts into spinner flasks in proliferation medium[17], where they self-assembled in three dimensions into SkMOs[25]. After 20 d, we reduced the serum concentration and allowed the cells to differentiate. After an additional 10 d, the SkMOs were predominantly composed of cells that expressed myosin heavy chain (MyHC), a marker for terminally differentiated myotubes[26], and cells that expressed Pax7, many of which were present near myotubes (Fig. 1a,b). Although MyoD was expressed in the vast majority (98% ± 0.70%) of the Pax7+ myoblasts used to generate SkMOs, it was expressed in only a small percentage (9% ± 4.28%) of the Pax7+ cells present in late-stage SkMOs (Fig. 1c,d).

To validate our findings, we used a transgenic *Pax7nGFP* reporter mouse strain (*Tg:Pax7nGFP*)[27] to FACS purify satellite cells (>95% GFP+) and derive, in standard two-dimensional (2D) growth conditions, several primary myoblast lines subsequently used to generate SkMOs (Supplementary Fig. 1a,b). After 30 d of organoid culture, GFP+ cells accounted for 18% ± 2% of the mononuclear cells within each organoid (Supplementary Fig. 1c). This provided approximately 3 ± 1.5 million GFP+ cells per spinner flask (Supplementary Fig. 1d). Finally, we compared the presence of canonical myogenic cell surface markers among myoblasts, SkMO GFP+ cells and freshly isolated satellite cells (Supplementary Fig. 1e) and found that SkMO GFP+ cells closely resembled the profile of satellite cells (Cxcr4+, CD104− and CD200+)[28].

In intact muscle, satellite cells are normally quiescent. Although the parental myoblasts used to form SkMOs incorporated the nucleoside analogue 5-ethynyl-2′-deoxyuridine (EdU) (93% ± 4.20% EdU+), indicative of cycling cells, very few Pax7+ cells (3% ± 1.5% EdU+) present in late-stage SkMOs were EdU+ (Fig. 1e,f). Additionally, a quiescent satellite cell can be distinguished from an activated satellite cell by cell size alone[29,30]. Consistent with those findings, FACS-sorted late-stage

SkMO-derived GFP+ cells were significantly smaller (9.15 ± 0.17 μm in diameter) than FACS-sorted GFP+ myoblasts (15.39 ± 0.68 μm), more closely resembling freshly isolated GFP+ primary satellite cells (6.76 ± 0.05 μm) (Fig. 1g,h). To further confirm that SkMO GFP+ cells have acquired properties of satellite cells, we set up a clonal growth assay modified from those used frequently to ascertain stem cell function in the neural and hematopoietic fields[31–34]. Using FACS to sort one GFP+ cell per well of a 96-well spheroid plate, we quantified the ability of freshly isolated Pax7nGFP satellite cells, myoblasts (derived from the satellite cells in two dimensions) and SkMO-derived GFP+ cells to form colonies in suspension (Supplementary Fig. 2a). After the confirmation that a single cell resided per well after 24 h in culture (Supplementary Fig. 2b), we found that freshly isolated satellite cells and SkMO-derived GFP+ cells, but not myoblasts, could form distinct clones (≥3 cells in a colony) (Supplementary Fig. 2c,d). Quantification of the approximate number of cells per clone revealed that satellite cells and SkMO-derived GFP+ cells gave rise to an average of 12.5 ± 0.9 cells per well and 6.9 ± 1.5 cells per well, respectively, whereas myoblasts rarely proliferated under these conditions (1.18 ± 0.16 cells per well) (Supplementary Fig. 2d). The regenerative properties of SkMO GFP+ cells were further illustrated by their ability to expand the number of SkMOs when passaged in spin culture (Supplementary Fig. 2e). Finally, we found that purified SkMO-derived GFP+ cells, as would be expected, retained their capacity to give rise to proliferative myoblasts capable of fusing to form multinucleated myotubes when cultured under standard differentiation conditions in vitro (Supplementary Fig. 2f).

Thus, using multiple criteria, including loss of MyoD expression, quiescence, cell size and clonal growth, combined with the ability to form differentiated muscle, it appears as if a population of cells resembling satellite cells arises when myoblasts are cultured in organoid-like conditions. For the remainder of this manuscript, we refer to SkMO-derived GFP+ cells as idSCs.

Satellite cells and idSCs share transcriptional similarities

To study transcriptional changes that define idSCs as they arise in myoblast-seeded organoids, we conducted multiplexed RNA sequencing (RNA-seq) analyses (3′ DGE) of freshly isolated satellite cells, myoblasts and idSCs, all derived from the *Tg:Pax7nGFP* mouse. We further obtained Pax7+ reserve cells, which are present in small numbers after traditional 2D differentiation in vitro of *Tg:Pax7nGFP* myoblasts into myotubes, as they represent the closest in vitro analogue to satellite cells[35,36] (Supplementary Fig. 3a). A focused analysis of genes known to be involved in satellite cell maintenance/activation[11] clustered idSCs with endogenous satellite cells while clearly distinguishing them from both myoblasts and reserve cells (Fig. 2a). Among the genes separating idSCs and satellite cells from myoblasts were genes associated with the Notch signaling pathway (*Notch3*, *HeyL* and *Jag1*), early activation/stress response (*Fos*, *Egr1* and *Socs3*), quiescence (*Spry1*, *Gas1* and *Timp3*), cell surface (*Cdh15*, *Cxcr4* and *Fgfr4*), extracellular matrix (ECM) (*Dcn*, *Dag1* and *Col15a1*) and secreted growth factors (*Igf1*, *Bmp4* and *Wnt4*). Quantitative polymerase chain reaction (qPCR) measurements and transcripts per million (TPM) analysis from our bulk RNA-seq dataset confirmed many of these findings (Supplementary Fig. 3b,c).

We then filtered this RNA-seq dataset based on differentially expressed genes (false discovery rate (FDR) < 0.1) between myoblasts and satellite cells (Supplementary Table 1), myoblasts and idSCs (Supplementary Table 2) or idSCs and satellite cells (Supplementary Table 3). Next, we conducted unbiased hierarchical clustering to analyze genes within a given clade according to KEGG pathway and curated gene groups. idSCs and satellite cells shared transcriptional patterns observed in clades (7, 4, 1, 3, 9, 8) broadly associated with a reduction in transcription, translation, cell cycle progression and metabolism, along with increases in quiescence, stress response and HDAC activity (Supplementary Fig. 3d and Supplementary Table 4). idSCs and myoblasts differed from satellite cells in clades (10, 11, 12, 13), which
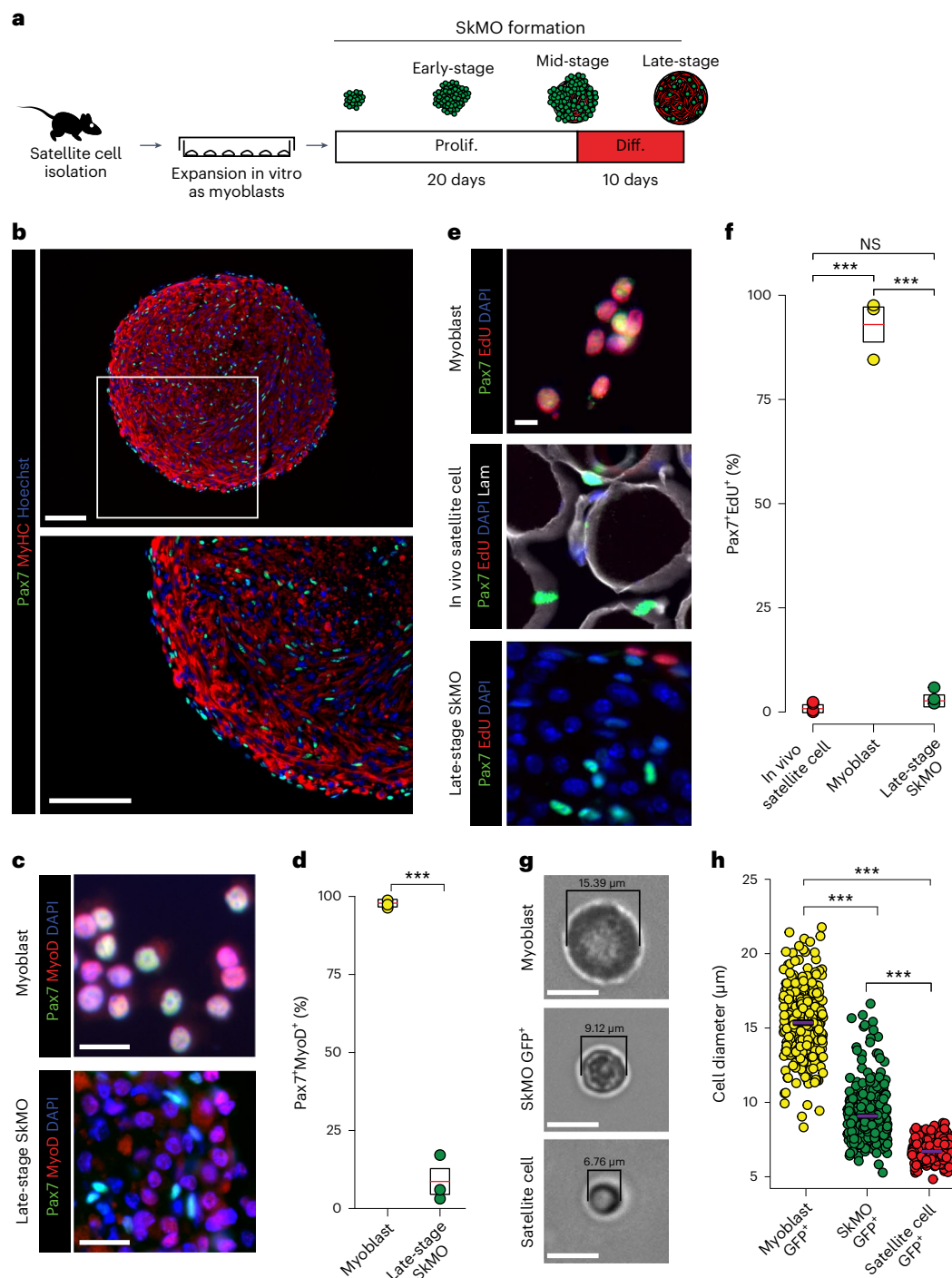
Fig. 1 | Mouse myoblasts can form SkMOs that share in vitro characteristics with satellite cells. a, Schematic of the isolation and expansion of mouse myoblasts in vitro followed by the formation, growth and maturation of an SkMO. **b**, Immunofluorescent images of a late-stage SkMO stained with Pax7 (green), MyHC (red) and nuclear counterstain Hoechst (blue). Scale bars, 100 μm. **c**, Immunostaining of myoblasts and late-stage SkMOs for MyoD (red), Pax7 (green) and Hoechst (blue). Scale bars, 20 μm. **d**, Percentage of Pax7+MyoD+ cells in myoblasts and late-stage SkMOs. Box bounds represent s.e.m.; red line represents mean ($n = 3$, biological replicates). Student's two-tailed t-test, unpaired with equal variance assumed and no multiple testing correction. P value: Myo versus SkMO 3.37×10^{-5}; ***$P < 0.001$. **e**, Immunofluorescent images from EdU pulse chase experiments over 48 h comparing myoblasts, quiescent satellite cells and late-stage SkMO cells. Images show Pax7 (green), EdU (red) and Hoechst (blue). Scale bars, 10 μm. **f**, Percentage of Pax7+EdU+ cells in each

cell condition. Box bounds represent s.e.m.; red line represents mean (satellite cell $n = 4$, myoblast $n = 3$, SkMO $n = 3$, biological replicates). Student's two-tailed t-test, unpaired with equal variance assumed and no multiple testing correction between samples. P values: SC versus SkMO 0.205, SC versus Myo 2.0×10^{-6}; Myo versus idSC 3.5×10^{-5}; ***$P < 0.001$. **g**, Representative images of myoblasts, SkMO-derived GFP+ cells and quiescent satellite cells immediately after FACS isolation. Scale bars, 10 μm. **h**, Comparisons of cell diameter in proliferative myoblasts, SkMO-derived GFP+ cells and quiescent satellite cells. Box bounds represent s.e.m.; red line represents mean ($n = 3$, biological replicates with ≥100 cells per replicate). Student's two-tailed t-test, unpaired with equal variance assumed and no multiple testing correction between samples. P values: Myo versus SC 2.22×10^{-4}; Myo versus SkMO 8.98×10^{-4}; SkMO versus SC 1.7×10^{-4}; ***$P < 0.001$. NS, not significant; Myo, myoblast; SC, satellite cell.
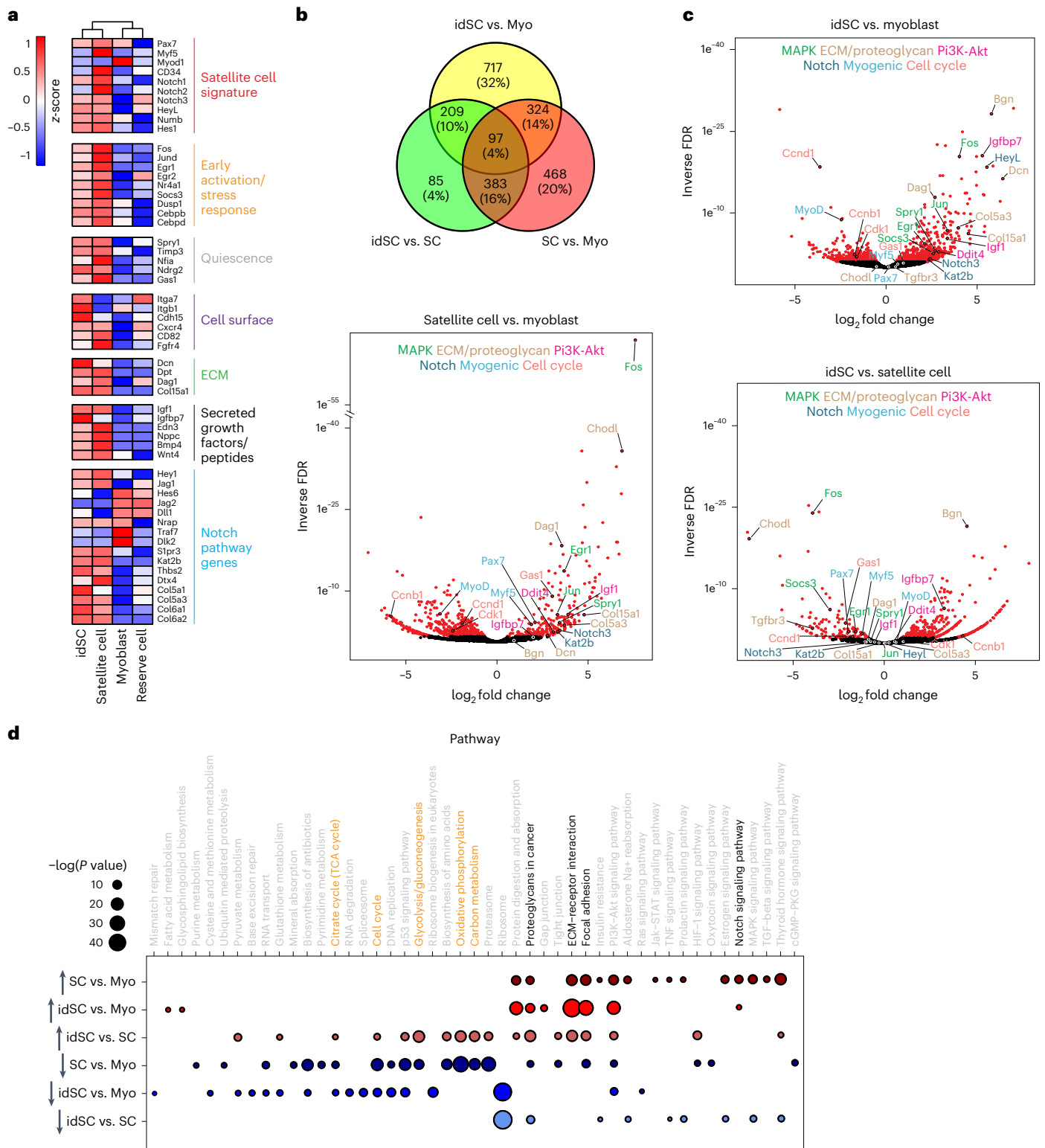
Fig. 2 | idSCs share key transcriptional similarities with satellite cells.
a, Heatmap depicting genes key to satellite cells, early activation and stress response, quiescence, cell surface receptors, ECM, secreted growth factors and Notch pathway genes colored based on z-score from high (red) to low (blue) (*n* > 4). **b**, Venn diagram depicting significant genes (FDR ≤ 0.1) among myoblasts, idSCs and satellite cells. **c**, Volcano plots depicting log₂ fold change in gene expression between satellite cells versus myoblasts (bottom left), idSCs versus

myoblasts (top right), and idSCs versus satellite cells (bottom right). Genes that are significant (FDR ≤ 0.1) are shown in red. **d**, KEGG pathways identified based on comparing differentially expressed genes among myoblasts, idSCs and satellite cells and visualized based on significance using a hypergeometric test (−log(*P* value)). Highlighted pathways are directly referenced in the text. Myo, myoblast; SC, satellite cell.

represent KEGG pathways involved in oxidative phosphorylation, proteosome activation and carbon metabolism, suggesting that idSCs have a shared, yet distinct, transcriptional profile with respect to myoblasts and satellite cells.

We next conducted differential gene expression analysis (FDR < 0.1) comparing satellite cells, idSCs and myoblasts to further characterize changes that occur at the transcriptional level. We identified 1,347 differentially expressed genes between idSCs and myoblasts, 1,272 genes differentially expressed between satellite cells and myoblasts and only 774 genes differentially expressed between idSCs and satellite cells (Fig. 2b). Volcano plots depicting differentially expressed genes among idSCs, satellite cells and myoblasts confirmed these findings and further demonstrated conserved trends in gene expression between satellite cells and idSCs (Fig. 2c). Functional enrichment analysis identified KEGG pathways for focal adhesion, ECM–receptor interactions, proteoglycans in cancer and the Notch signaling pathway as being conserved and upregulated in idSC and satellite cell samples relative to myoblasts (Fig. 2d). Conversely, myoblasts and idSCs are more similar with respect to their increased activation of KEGG pathways broadly involved in cell cycle and a variety of metabolic pathways (glycolysis, OxPhos, carbon and tricarboxylic acid (TCA) cycle) when compared to satellite cells (Fig. 2d). These data suggest that idSCs are intermediate with respect to their transcriptional profile when compared to both myoblasts and satellite cells.

Epigenomic changes regulate/underlie idSC formation

The organization of the epigenome with respect to chromatin structure is a major regulator of stem cell identity[37,38]. We reasoned that a temporal analysis of chromatin dynamics would provide insight into the process by which idSCs are generated when myoblasts are grown in an organoid format. We conducted Omni-ATAC-seq[39] to measure changes in the epigenome during the generation of idSCs within SkMOs at early (day 10), mid (day 20) and late (day 30) timepoints (Supplementary Fig. 4a). An initial correlation heatmap distinguished early-stage, mid-stage and late-stage idSC samples from satellite cells and from their parental myoblast lines (Supplementary Fig. 4b). We observed dynamic patterns of change in chromatin accessibility among proliferative myoblasts, idSCs present in SkMOs at the three different timepoints and freshly isolated satellite cells. These regions (or peaks) existed across the spectrum of open and closed chromatin, and we identified approximately 40,000 myogenic responsive chromatin regions (adjusted P < 0.0001, Wald test)[40] that differed after pairwise comparison among the five cellular states. Unbiased hierarchical clustering identified five clades (1.1, 1.2, 2.1, 2.2 and 3) that distinguished the myogenic responsive chromatin regions. Association of chromatin peaks present in each clade to candidate gene and Gene Ontology (GO) terms was conducted using the Genomic Regions Enrichment of Annotations Tool (GREAT)[41]. Clades 1.1 and 1.2 included peaks that were primarily open in myoblasts (myoblast state) and closed in satellite cells and in idSCs starting at day 10 onward (Fig. 3a, dashed box). Peaks found in these clades were enriched for GO Biological Processes (GO BPs) involved in striated muscle development (*Actin*, *Atg5/7*, *Lmod3*, *MyoG*, *Prox1* and *Pitx2*), contraction (α and β adrenergic receptors, *Calm1*, *Prok2*, *Ttn* and Na/K channel genes), myotube differentiation (*MyoD*, *MyoG*, *Myocd*, *Cyp26b1* and *Cxcl12*) and histone citrullination (Padi gene family) (Fig. 3a,b and Supplementary Table 5). Clade 2.1 is shared between myoblast and mid- to late-stage idSC samples (transition state) and includes GO BPs involved in vascular development (*Tcf4*, *Dcn*, *Fgf1*, *Ets1* and *Btg1*) and cytokine production (*Runx1*, *Fn1*, *Pik3r1*, *Thbs1*, *Csf1r*, *Trib2*, *Foxp1*, *Smad7* and *Smad3*). Clade 2.2, which is unique to mid-stage and late-stage idSC samples, represents GO BPs involved in actin cytoskeleton organization (*Nrp1*, *Actn1*, *Foxp1* and *Tpm1*) and ECM organization (*Col5a1*, *Dpt*, *Grem1* and *Has1*). Finally, clade 3, which was predominantly open in satellite cells (satellite cell state) and closed in other samples, is associated with genes involved in

regulation of carbohydrate metabolism (*Foxo1*, *Irs2*, *Prkce* and *Rora*), cellular response to insulin stimulus (*Errfi1*, *Foxo1*, *Pik3r1* and *Zfp36l1*) and negative regulation of cell cycle phase transition (*Zfp36l1*, *Zfp36l2*, *Foxn3* and *Cradd*) (Fig. 3a,b and Supplementary Table 5). We observed a progressive closure of chromatin accessibility for myoblast state peaks in a temporal fashion across idSC timepoints (early, mid and late stage), ultimately resulting in closed chromatin in satellite cells (Fig. 3a, dashed box). Unbiased pathway analysis involving differential binding (DiffBind) comparisons among myoblasts, day 30 idSCs and satellite cells identified candidate signaling pathways for genes found in open chromatin unique to satellite cells (VEGF signaling, vascular smooth muscle contraction and Tgfβ signaling), shared between myoblasts and day 30 idSCs (Jak/Stat, insulin and mTOR signaling pathways) and candidate pathways shared by both day 30 idSCs and satellite cells (regulation of actin cytoskeleton, MAPK signaling, leukocyte trans-endothelial migration and focal adhesion) (Supplementary Fig. 4c). These broad genome-wide changes suggest that idSCs transition over time to silence the myoblast epigenomic state, in line with satellite cells, yet maintain a unique chromatin profile linked to ECM and actin remodeling.

To further study whether epigenetic similarities exist between idSCs and satellite cells, we next conducted a pairwise comparison to identify peaks that are open in both late-stage idSCs and satellite cells and closed in myoblasts (Fig. 3c). GREAT analysis of this refined list of peaks identified GO Cellular Components involved in ECM and cytoskeletal signaling (D*cn*, *Tgfbr3*, *Dag1* and *Timp3*)[42,43] and collagen deposition, most prominently collagen V trimers (*Col5a1*, *a2*, *a3*, *Col6a1* and *Col6a2*), known to promote satellite cell function[44], along with other collagens present in the satellite cell niche (*Col15a1* and *Col27a1*)[43,45] (Fig. 3d). Further examination of candidate genes known to regulate satellite cell fate identified chromatin closure at the *MyoD* and *MyoG* loci (Supplementary Fig. 4d) conserved between late-stage idSCs and satellite cells[8]. Conversely, we observed open chromatin surrounding Notch pathway members, as well as TFs associated with the satellite cell state, in idSC timepoints and satellite cells (Supplementary Fig. 4d). These data highlight the involvement of key ECM molecules, found in the satellite cell niche, as well as Notch signaling, in orchestrating the process by which idSCs arise when myoblasts are cultured in organoid format.

In accordance with other cell types undergoing dedifferentiation, initial transcriptional and epigenomic downregulation of the myogenic program might be expected to occur early in the process, followed by activation of genes highly expressed in satellite cells. We examined whether specific TF binding motifs differed between each distinct cellular state, therefore allowing us to predict TF regulatory networks that characterize the transition from myoblast to idSC. We used chromVAR to calculate a genome-wide chromatin variability score and found that the most dynamically regulated TF binding sites across all samples were predominantly members of the basic leucine zipper (bZip) or basic helix-loop-helix (bHLH) TF families (Supplementary Fig. 4e). These dynamic binding sites include the canonical myogenic bHLH TFs (*MyoD*, *Myf5*, *Myog* and *Myf6*), along with bZIP TFs, including several members of the activator protein (AP-1) complex. Given that TF binding sites present in open chromatin suggest active transcriptional regulation by the cognate TF, we conducted transcription factor occupancy prediction by investigation of ATAC-seq signal (TOBIAS)[46] to establish whether a given TF is bound at a specific site. As *MyoD* is a master TF that regulates myogenic identity, we analyzed myoblast-specific peaks that contained consensus *MyoD* binding sites that were bound (footprint) using TOBIAS, and then we associated these bound peaks with their nearest gene using GREAT and identified GO BP terms enriched for skeletal muscle fusion/contraction (Fig. 3e). We subsequently asked whether these peaks remain bound in satellite cells and in idSCs. We observed a notable temporal reduction in TF occupancy on *MyoD* sites normally bound in myoblasts, such that late-stage idSCs and satellite cells were essentially unbound (Fig. 3f),
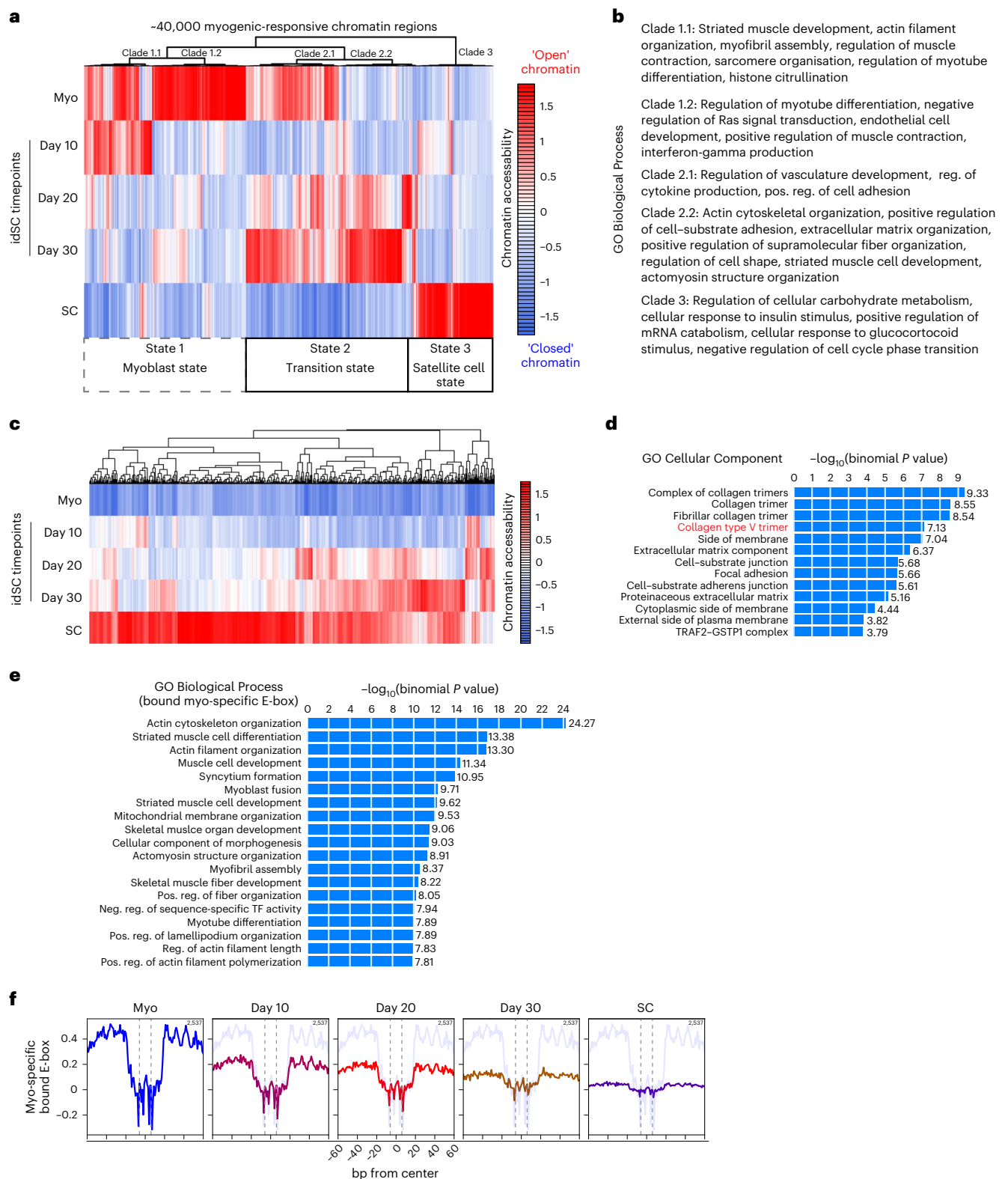
Fig. 3 | Key regulatory regions in myoblasts that define the myogenic program are silenced during idSC generation. a, Heatmap depicting dynamic patterns of change in chromatin accessibility that occur between proliferative myoblasts and idSCs at early-stage (day 10), mid-stage (day 20) or late-stage (day 30) culture timepoints and freshly isolated satellite cells. Clustering of peaks into three broad states: myoblast specific, transition state specific and satellite cell specific. Boxed region highlights myoblast specific peaks in an open configuration remodeled into closed chromatin during idSC formation. **b**, Clade analysis with associated GO BP terms generated by GREAT based on an unbiased dendogram depicting similarities in chromatin accessibility across sample types. **c**, Heatmap depicting dynamic patterns of change in chromatin accessibility conserved between late-stage idSCs and satellite cells relative to myoblasts. **d**, Associated GO Cellular Component terms for genes with *cis*-regulatory peaks conserved between late-stage idSCs and satellite cells using a binomial test. **e**, Associated GO BP terms for genes with *cis*-regulatory bound E-box sites specific to myoblasts using a binomial test. **f**, Footprinting of E-box sites bound in myoblasts across idSC samples and satellite cells. Example shows progressive loss in accessibility over time in cultured idSCs, similar to satellite cell footprinting. SC, satellite cell.

further supporting our findings that idSCs have reduced expression of *MyoD* protein and RNA (Figs. 1c,d and 2a,c).

These data underscore the closure of chromatin regulating the broad myogenic program, with specific evidence demonstrating that bound *MyoD* consensus sites are remodeled into closed chromatin during the appearance of idSCs in organoids, making them more similar to what is observed in satellite cells. For these reasons, we decided to compare the in vivo capacity of late-stage (day 30) idSCs to both myoblasts and freshly isolated satellite cells in vivo.

idSCs regenerate muscle on par with satellite cells

Cell functionality is traditionally determined by cell transplantation. To test the in vivo behavior of late-stage idSCs, we infected primary myoblast lines from *Tg:Pax7[nGFP]* reporter mice with a lentivirus expressing luciferase and tdTomato (LT). This dual reporter facilitated FACS isolation of nGFP⁺tdTomato⁺ cells and the detection of donor-derived cells in histological sections, along with the ability to carry out longitudinal in vivo monitoring of transplanted cells using bioluminescent imaging (BLI)[47,48]. We induced bilateral cardiotoxin (CTX) injuries in the left and right tibialis anterior (TA) muscles of immunodeficient NSG mice. This allowed us to test in parallel two different types of cells in the same animal, thereby reducing experimental variability[49]. Forty-eight hours after injury, we transplanted 10,000 nGFP⁺tdTomato⁺ idSCs or nGFP⁺tdTomato⁺ parental myoblasts into regenerating TA muscles (Fig. 4a and Supplementary Fig. 5a). We subsequently conducted BLI measurements at 7 d, 14 d and 21 d after transplant to determine the persistence of engrafted cells (Fig. 4b and Supplementary Fig. 5b). Both myoblasts and idSCs displayed detectable radiance 48 h after transplant, confirming the success of the procedure (Supplementary Fig. 5c). However, at later timepoints, the radiance associated with transplanted idSCs progressively increased, whereas myoblast radiance levels steadily decreased (Fig. 4b). After 21 d, we observed a significant increase in radiance from TA muscles transplanted with idSCs (3.2 ± 0.7 million photons cm⁻² s⁻¹) compared to myoblasts (0.007 ± 0.001 million photons cm⁻² s⁻¹). This was observed even when a 50-fold excess of myoblasts was transplanted (Supplementary Fig. 5d). These data show that idSCs efficiently persist after transplantation, whereas myoblasts, in line with previous findings, do not[14,50].

To explore the capacity of transplanted cells to incorporate into regenerating muscle fibers, we sectioned and stained TA muscles for the presence of tdTomato within myofibers from mice previously imaged by BLI. Under these conditions, donor cells and endogenous host satellite cells are competing to generate new myofibers. Manual injection of cells as well as differences in the area of damage produced by CTX in individual muscles contribute to variability. Notwithstanding,

we observed significant engraftment of idSCs compared to myoblasts 21 d after transplant of 10,000 cells into CTX-damaged TA muscles (Fig. 4c). We further quantified this engraftment across entire muscle sections, finding that idSCs gave rise, on average, to $5.8\% \pm 0.8\%$ tdTomato⁺ fibers per section (193.60 ± 27.01 tdTomato⁺ fibers per section), whereas myoblasts only rarely gave rise to engrafted fibers ($0.02\% \pm 0.02\%$ or 0.80 ± 0.80 tdTomato⁺ fibers per section) (Fig. 4d).

To confirm the ability of idSCs to repopulate the satellite cell niche, we stained transplanted muscle sections to identify donor-derived cells defined by the expression of both Pax7 and tdTomato (Fig. 4e). We found that idSCs gave rise to 44.8 ± 10.76 Pax7⁺tdTomato⁺ cells per section. When compared to the total number of Pax7⁺ cells in muscle sections, idSCs accounted for $14\% \pm 4\%$ of Pax7⁺tdTomato⁺ cells. In contrast, myoblasts produced a negligible number of Pax7⁺tdTomato⁺ cells, expressed either as a total (0.4 ± 0.24) or as a percentage ($0.2\% \pm 0.1\%$) (Fig. 4f). Taken together, these data suggest that idSCs have acquired the capacity to repopulate the stem cell niche and strongly resemble satellite cells after transplant into damaged muscle.

To determine whether idSCs can self-renew after damage, we subjected NSG mice, that had previously been transplanted bilaterally with 10,000 myoblasts or idSCs, to two additional rounds of re-injury conducted at days 21 and 42 after transplant (Fig. 4a). Successful self-renewal of these transplanted cells would allow them to participate in muscle repair after multiple rounds of injury. After each episode of CTX-induced injury, we observed enhanced radiance from TA muscles transplanted with idSCs (228 ± 84 million photons cm⁻² s⁻¹ at 42 d and 3.09 ± 1.2 billion photons cm⁻² s⁻¹ at 63 d) (Fig. 4g and Supplementary Fig. 5e). This significant increase in radiance levels after re-injury was observed only in the idSC samples and not in TAs transplanted with parental myoblasts. To further confirm that idSCs were able to support muscle regeneration after injury, we evaluated sectioned muscle for the presence of donor-derived fibers (tdTomato⁺) after one round of re-injury (day 42). Donor-derived fibers were readily observed in idSC-transplanted muscle, whereas they were completely absent in myoblast-transplanted samples (Fig. 4h). After one round of re-injury, idSCs contributed to the formation of new myofibers ($43\% \pm 10\%$ tdTomato⁺ fibers) across the entire muscle section, whereas no discernable tdTomato⁺ fibers were observed after re-injury of TA muscles transplanted with 10,000 myoblasts (Fig. 4i). These findings differ substantially from transplanted muscle that is not re-injured (Supplementary Fig. 5f), underscoring the capacity of idSCs to self-renew, giving rise to cells able to engraft into muscle and repopulate the satellite cell niche.

To rigorously compare unmodified freshly isolated satellite cells, idSCs and myoblasts, we assessed engraftment, repopulation and self-renewal of transplanted cells in a mouse model of muscular

---

Fig. 4 | idSCs engraft, repopulate and self-renew in vivo. a, Experimental schematic outlining the transplant and analysis of myoblasts or idSCs into regenerating TA muscle of NSG mice. **b**, Quantification of the average radiance (photons cm⁻² s⁻¹) across a standardized region of interest (ROI) superimposed over NSG hindlimbs over a 21-d timecourse after transplant of 10,000 myoblasts (yellow) or idSCs (green). Data represent mean ± s.e.m ($n = 97$ day 7; $n = 102$ day 14; $n = 92$ day 21, biological replicates). Student's two-tailed *t*-test, unpaired with equal variance assumed and no multiple testing correction. *P* values: day 7 0.011; day 14 5.23×10^{-6}; day 21 5.40×10^{-5}; *P* < 0.05, ***P* < 0.001. **c**, Representative immunofluorescence micrograph depicting engraftment after the transplant of nGFP⁺tdTomato⁺ myoblasts or idSCs into newly regenerated muscle of NSG mice. Images were stained with laminin (green), tdTomato (red) and Hoechst (blue). Scale bar, 100 μm. **d**, Quantification of the percentage of tdTomato⁺ fibers per muscle cross-section after transplant of either myoblasts or idSCs. Box bounds represent s.e.m.; bar represents mean ($n = 5$, biological replicates). Student's two-tailed *t*-test, unpaired with equal variance assumed and no multiple testing correction. *P* value: idSC versus Myo 6.70×10^{-5}; ***P* < 0.001. **e**, Representative immunofluorescent micrograph depicting the ability of donor-derived cells to repopulate the satellite cell niche and express Pax7 (green), tdTomato (red) and Hoechst (blue). Arrowheads represent sublaminar Pax7⁺tdTomato⁻ cells within

NSG mice. Arrows indicate sublaminar Pax7⁺tdTomato⁺ cells. Scale bar, 100 μm. **f**, Quantification of the percent of sublaminar Pax7⁺tdTomato⁺ cells relative to the total Pax7⁺ cells per section. Percent double-positive cells was derived from an average total of Pax7⁺tdTomato⁺ to Pax7⁺ cells quantified per replicate (shown in panel). Box bounds represent s.e.m.; bar represents mean ($n = 5$, biological replicates). Student's two-tailed *t*-test, unpaired with equal variance assumed and no multiple testing correction. *P* value: idSC versus Myo 7.24×10^{-3}; ***P* < 0.01. **g**, 63-d longitudinal BLI study examining engraftment of 10,000 idSCs or myoblasts, followed by re-injury of muscle at 21 d and 42 d after transplant. Data represent mean ± s.e.m. ($n = 18$, days 21, 28, 35 and 42; $n = 15$, days 44, 49, 56 and 63; $n = 3$, day 23, biological replicates). Student's two-tailed *t*-test, unpaired with equal variance assumed and no multiple testing correction. *P* values: day 21, 0.005; day 23, 0.077; day 28, 0.001; day 35, 0.001; day 42, 0.015; day 44, 0.019; day 49, 0.024; day 56, 0.044; day 63, 0.030; *P* < 0.05, ***P* < 0.01, ****P* < 0.001. **h**, Immunofluorescence micrograph of a TA cross-section before the second round of re-injury (day 42). tdTomato⁺ (red) and laminin (green). Scale bars, 500 μm. **i**, Percentage of tdTomato⁺ fibers per muscle section ($n = 3$, biological replicates). Box bounds represent s.e.m.; red line represents mean. Student's two-tailed *t*-test, unpaired with equal variance assumed and no multiple testing correction. *P* value: Myo versus idSC 0.012; *P* < 0.05. Myo, myoblast.

dystrophy (mdx^{Scv}) in which muscle recovery from damage is impaired and revertant myofiber frequency is low (Fig. 5a)[51]. We found that the ability of idSCs to engraft (9.6% ± 1.3% dystrophin+ fibers per section) was as good as, if not superior to, that of freshly isolated satellite cells (7.3% ± 1.07% dystrophin+ fibers per section) (Fig. 5b,c). After re-injury, idSC engraftment appeared better than that achieved with freshly isolated satellite cells (21.5% ± 3.78% dystrophin+ fibers per section and 7.4% ± 4.1% dystrophin+ fibers per section, respectively) (Fig. 5c). Furthermore, the number of cells repopulating the satellite cell niche was similar at day 21 (9.9% ± 2.1% of Pax7+nGFP+ cells for idSCs and 10.9% ± 2.5% of Pax7+nGFP+ cells for satellite cells), whereas day 42 displayed a greater degree of repopulation for idSCs relative to satellite cells (28.2% ± 3.5% of Pax7+nGFP+ cells and 12.9% ± 3.2% of Pax7+nGFP+ cells, respectively) (Fig. 5d,e). At day 42, after re-injury, most of both populations (70.9% ± 8.9% of idSCs and 51.8% ± 7.7% of satellite cells) have withdrawn from the cell cycle and are Pax7+nGFP+Ki67− (Fig. 5f,g).

As expected, donor myoblasts were unable to engraft or repopulate the satellite cell niche in damaged mdx^{Scv} muscle (0.31% ± 0.1% dystrophin+ fibers per section and 0.7% ± 0.3% of Pax7+nGFP+ cells) and, when proliferated in vitro, were rarely Pax7+nGFP+Ki67− (13.5% ± 4.1%) (Supplementary Fig. 6a,b). Together, these data indicate that, despite being somewhat different from satellite cells based on transcriptional and epigenomic signatures, the in vivo behavior of transplanted idSCs is nearly equivalent to that of bona fide satellite cells.

idSCs restore muscle function on par with satellite cells

To determine whether transplanted idSCs could improve the function of damaged muscle, another test of their similarity to satellite cells, we irradiated TA muscles of NSG mice (13 Gy), induced damage with CTX and subsequently transplanted 10,000 myoblasts, idSCs or satellite cells (Fig. 6a). Irradiation of hindlimb muscle prevents endogenous satellite cells from entering the cell cycle after muscle damage[52], meaning
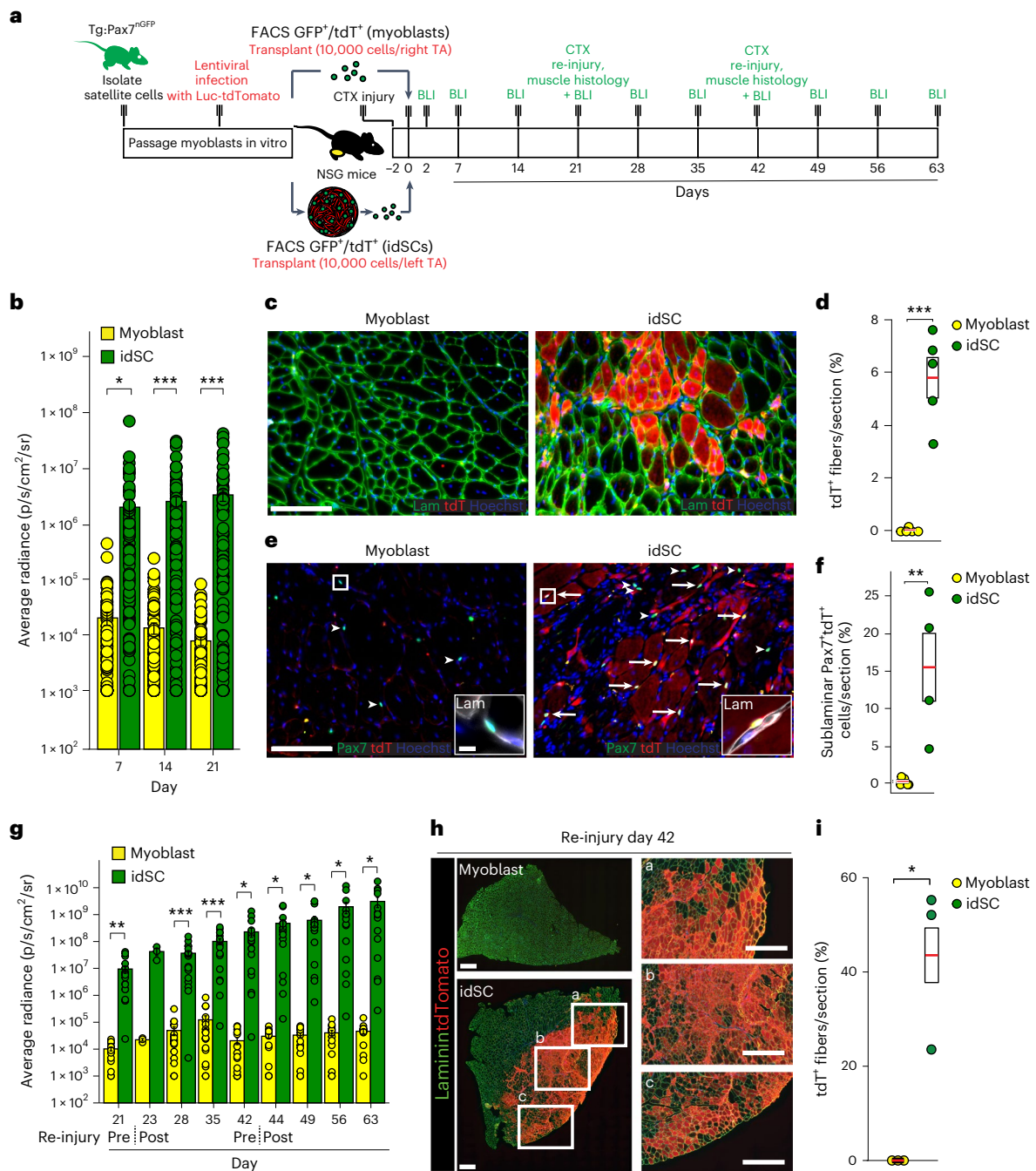
that the only cells capable of repairing muscle would be those provided by transplantation. We observed a substantial difference in specific force production between transplanted idSCs and myoblasts. idSCs gave rise to 138 ± 20.49 kN $\times$ m^{-2}, similar to that produced by satellite cells (178 ± 16.43 kN $\times$ m^{-2}), whereas myoblasts gave rise to negligible specific force readings (3 ± 0.88 kN $\times$ m^{-2}) (Fig. 6b). These findings were further supported when assessing maximum tetanic and twitch forces (Supplementary Fig. 7a–d). Muscle force data were strongly supported by histological evaluation of the treated muscle at the conclusion of the study (Fig. 6c) and by quantifying the total number of myofibers per section obtained after the transplant of either satellite cells or idSCs ($1,535 \pm 145$ fibers and $1,965 \pm 313$ fibers, respectively) (Fig. 6d). In contrast, sham (saline) and myoblast samples had much fewer fibers after regeneration (14 ± 8 fibers and 84 ± 12 fibers, respectively). These findings correlated with the percentage of centrally located nuclei in transplanted samples, a hallmark of newly regenerated muscle (Supplementary Fig. 7e), and with TA muscle weights (Supplementary Fig. 7f). Irradiated undamaged muscle was devoid of centrally nucleated myofibers consistent with the low levels of satellite cell turnover under normal conditions (Fig. 1f and Supplementary Fig. 7e). Finally, both idSCs and satellite cells reoccupied the satellite cell niche to a similar extent after regeneration (Supplementary Fig. 7g,h), further supporting the ability of late-stage idSCs to repopulate the satellite cell niche.

To purify idSCs without relying on a reporter, we considered the different expression of cell surface markers on idSCs and myoblasts (Supplementary Fig. 1e) and identified a combination of CD9$^+$ and CD104$^-$ that effectively isolates idSCs (Supplementary Fig. 8a). Validation against nGFP$^+$ idSCs resulted in $98.2\% \pm 2.2\%$ CD9$^+$CD104$^-$, whereas the converse CD9$^+$CD104$^-$ population contained $87.6\% \pm 6.6\%$ nGFP$^+$ cells (Supplementary Fig. 8a). We subsequently transplanted 10,000 CD9$^+$CD104$^-$ sorted cells into TA muscles previously irradiated and damaged with CTX (Supplementary Fig. 8b). CD9$^+$CD104$^-$ idSCs, when compared to nGFP$^+$ sorted idSCs, resulted in similar levels of muscle formation (Supplementary Fig. 8c), the presence of donor cells repopulating the satellite cell niche (Supplementary Fig. 8d) and similar mean specific force values (163 ± 22.7 kN $\times$ m^{-2} relative to nGFP$^+$ sorted 138 ± 20.49 kN $\times$ m^{-2}) (Supplementary Fig. 8e). In addition, mean maximum force values (Supplementary Fig. 8f), TA muscle weights (Supplementary Fig. 8g) and percentage of centrally located nuclei (Supplementary Fig. 8h) in nGFP$^+$ and CD9$^+$CD104$^-$ transplants were comparable.

Recapitulation of idSC formation in human SkMOs
To make our findings more clinically relevant, we obtained human myoblast lines from patient biopsies or purchased them from commercial sources. We subsequently generated human SkMOs in an enhanced serum-free medium containing well-characterized components and limited animal products using a shortened 15-d protocol (Supplementary Fig. 9a)[53]. We observed subtle differences between the expression of human myogenic cell surface markers assessed at the myoblast stage and after 15 d of SkMO culture (Supplementary Fig. 9b). Although variable between replicates, %PAX7$^+$ cells are rare across human myoblast lines ($3.5\% \pm 3\%$) (Supplementary Fig. 9c,d). After the formation of human SkMOs, the percentage of PAX7$^+$ cells decreases in variability across replicates and accounts for $5\% \pm 1\%$ of total cells (Supplementary Fig. 9c,d). Notably, whereas PAX7$^+$ cells in myoblasts are predominantly MYOD$^+$ ($84\% \pm 2\%$), in human SkMOs a minority are MYOD$^+$ ($5\% \pm 2\%$) (Supplementary Fig. 9c,e). Consistent with these findings, we observe a global decrease in the percentage of EdU$^+$ cells when transitioning from proliferating myoblasts to human SkMOs (Supplementary Fig. 9f,g), resulting in a reduction in the percentage of PAX7$^+$EdU$^+$ cells between myoblasts ($30\% \pm 22\%$) and human SkMOs ($0.8\% \pm 1.7\%$) (Supplementary Fig. 9h). These findings suggest that SkMO formation drives myoblast dedifferentiation across species to a quiescent state whereby Pax7 is maintained while MyoD expression is absent.

Discussion
To develop a cell-based therapeutic capable of repairing damaged muscle, a source of myogenic cells—autologous or not—must engraft, repopulate the satellite niche and self-renew such that they can repair muscle after multiple rounds of damage. Potential sources are adult myoblasts, satellite cells, embryonic stem (ES)-derived or induced pluripotent stem cell (iPSC)-derived myogenic progenitors and the cells that we describe in this paper—idSCs. In clinical trials, myoblasts have been safe yet ineffective[54–61]. To date, no clinical trials have enriched for Pax7$^+$ cells before transplant and have, rather, relied on the expression of N-CAM (CD56). Given that attempts to expand myoblasts in culture substantially reduces their effectiveness in vivo, a better understanding of the mechanisms responsible, along with rigorous transplant validation in vivo according to the standards set by satellite cells, are required[62–64]. In contrast, satellite cells, which have all the desirable criteria and, yet, are rare in postnatal skeletal muscle, necessitate methods to reliably expand them sufficiently to generate therapeutic numbers in vitro[50,64–68]. Alternatively, myogenic progenitors produced from embryonic (hESC or iPSC) stem cells show promise with respect to cell yield and can model both embryonic muscle formation[69] and neuromuscular development[70,71]. However, they remain in an immature state and do not demonstrate long-term regenerative capacity in vivo[69,72–76]. No myogenic cell has shown efficacy in the clinic, and the optimal cell source and culture protocol remain to be determined.


Fig. 5 | idSCs engraft, repopulate and self-renew in vivo in a dystrophin-deficient mouse model. a, Schematic summarizing isolation and transplant timelines. **b**, Representative immunofluorescence micrograph depicting engraftment after the transplant of 10,000 FACS-sorted nGFP$^+$ myoblasts, idSCs or freshly isolated satellite cells into irradiated (IRR) (13 Gy) TA muscles of *mdx^{Scv}* mice. Images were stained with dystrophin (green), laminin (red) and Hoechst (blue). Scale bar, 100 µm. **c**, Quantification of the percentage of dystrophin$^+$ fibers relative to the total laminin$^+$ fibers per muscle cross-section. Box bounds represent s.e.m.; bar represents mean (day 21: $n = 8$ Myo, $n = 10$ idSC, $n = 7$ SC; day 42: $n = 9$ idSC, $n = 4$ SC, biological replicates) One-way ANOVA with Tukey HSD analysis conducted at day 21 and day 42 between samples. Day 21 ANOVA P value 6.82×10^{-6}, Tukey HSD adjusted P values: day 21 idSC versus Myo 5.48×10^{-6}, day 21 idSC versus SC 0.292, day 21 Myo versus SC 6.26×10^{-4}; day 42 ANOVA P value 0.049. *$P < 0.05$, **$P < 0.01$, ***$P < 0.001$. **d**, Representative immunofluorescent micrograph depicting the ability of donor-derived cells to repopulate the satellite cell niche and express Pax7 (green), nGFP (red), laminin (white) and Hoechst (blue). Arrowheads represent sublaminar Pax7$^+$nGFP$^-$ (endogenous) satellite cells within *mdx^{Scv}* mice. Arrows indicate sublaminar Pax7$^+$nGFP$^+$ cells (donor derived). Scale bars, 100 µm. **e**, Quantification of the percent of sublaminar Pax7$^+$nGFP$^+$ cells per section. Box bounds represent s.e.m.; bar represents mean (day 21 $n = 8$ Myo, $n = 6$ idSC, $n = 7$ SC; day 42 $n = 8$ idSC, $n = 3$ SC, biological replicates). One-way ANOVA with Tukey HSD analysis conducted at day 21 and day 42 between samples. Day 21 ANOVA P value 7.31×10^{-4}, Tukey HSD adjusted P values: idSC versus Myo 4.73×10^{-3}, idSC versus SC 0.91, Myo versus SC 1.26×10^{-3}. Day 42 ANOVA P value 0.035. *$P < 0.05$, **$P < 0.01$, ***$P < 0.001$. Raw counts for the number of Pax7$^+$nGFP$^+$/total Pax7$^+$ are displayed at the top of the panel. **f**, Representative immunofluorescent micrograph depicting Pax7, nGFP, Ki67 and Hoechst. Arrows represent Pax7$^+$nGFP$^+$ cells (donor derived). Scale bars, 25 µm. **g**, Quantification of the percent of sublaminar Pax7$^+$nGFP$^+$Ki67$^-$ cells per section. Data represent mean ± s.e.m. ($n = 8$ idSC; $n = 5$ SC, biological replicates). Student's two-tailed t-test, unpaired with equal variance assumed and no multiple testing correction between samples. P value: SC versus idSC 0.166. Raw counts for the number of Pax7$^+$nGFP$^+$Ki67$^-$/total Pax7$^+$nGFP$^+$ are displayed at the top of the panel. HSD, honestly significant difference; NS, not significant; SC, satellite cell.

Our data show that culturing myoblasts in suspension under appropriate conditions stimulates their self-assembly into SkMOs and adheres to the founding principles established to describe organoids[77]. In fact, 3D cultures of cells from dissociated skeletal muscle exist and yet have been employed for other purposes and differ from SkMOs in that they contained non-myogenic lineages with few Pax7+ cells[78–82]. We showed that idSCs are expandable and can be derived from mouse tissue (Fig. 1) as well as from adult human commercial and non-commercial myoblast lines (Supplementary Fig. 9). The production of idSCs is both robust, in that they can be readily produced in the millions (Supplementary Fig. 1d), and reproducible

(Supplementary Figs. 1c and 9e), given their successful generation by numerous members of our research group using several different mouse strains. idSCs when transplanted into regenerating muscle engraft on par with satellite cells (Figs. 4 and 5) and approximate previous findings in the field[12,83]. In addition, idSCs repopulate the niche and self-renew in vivo in both unaffected and diseased models of muscle regeneration (Figs. 4 and 5). Of note, in the absence of endogenous satellite cells, idSCs give rise to de novo muscle fibers that generate force on par with transplanted satellite cells (Fig. 6 and Supplementary Fig. 7). Finally, we developed a purification strategy using cell surface markers for mouse idSCs that, when transplanted in vivo, yield similar
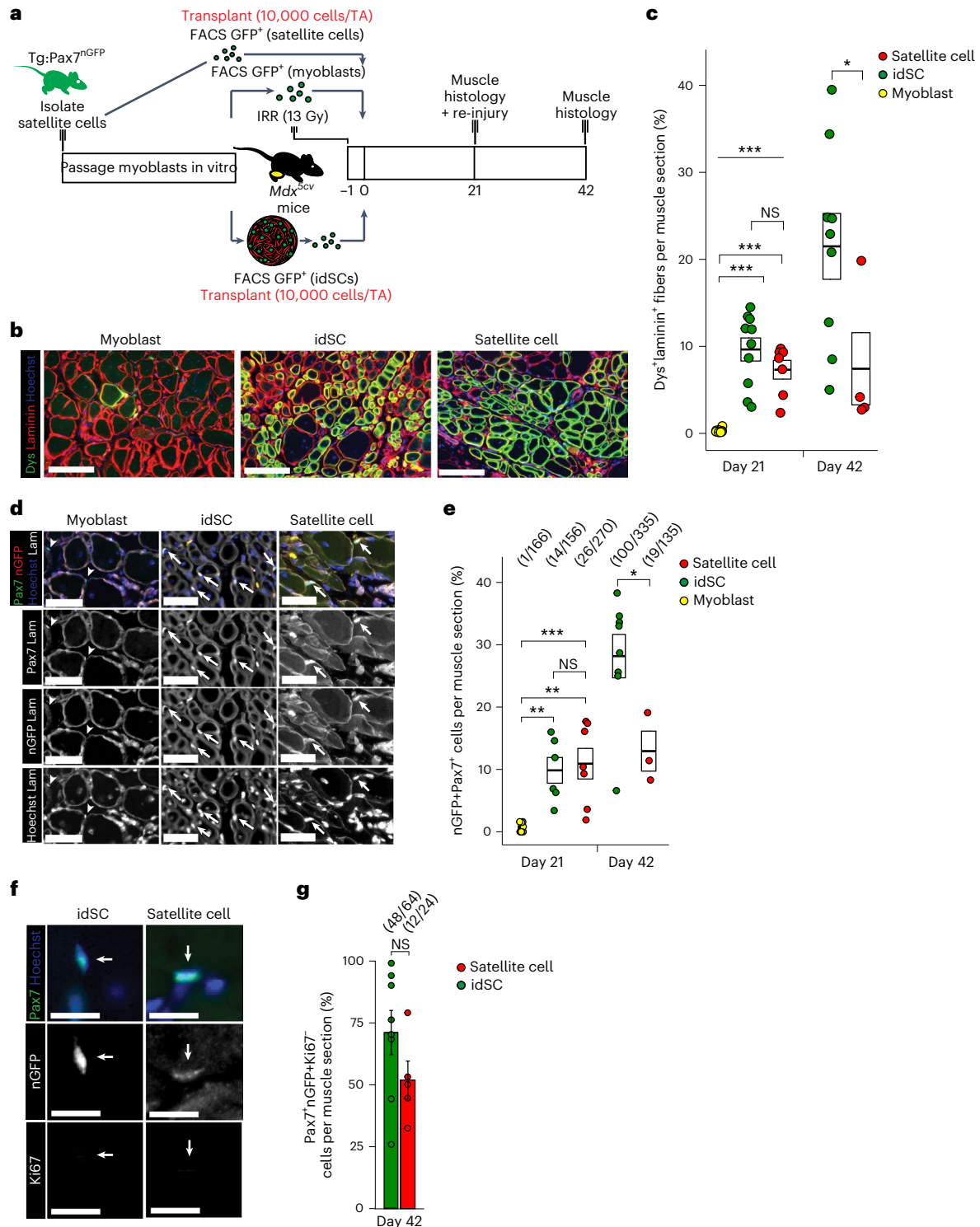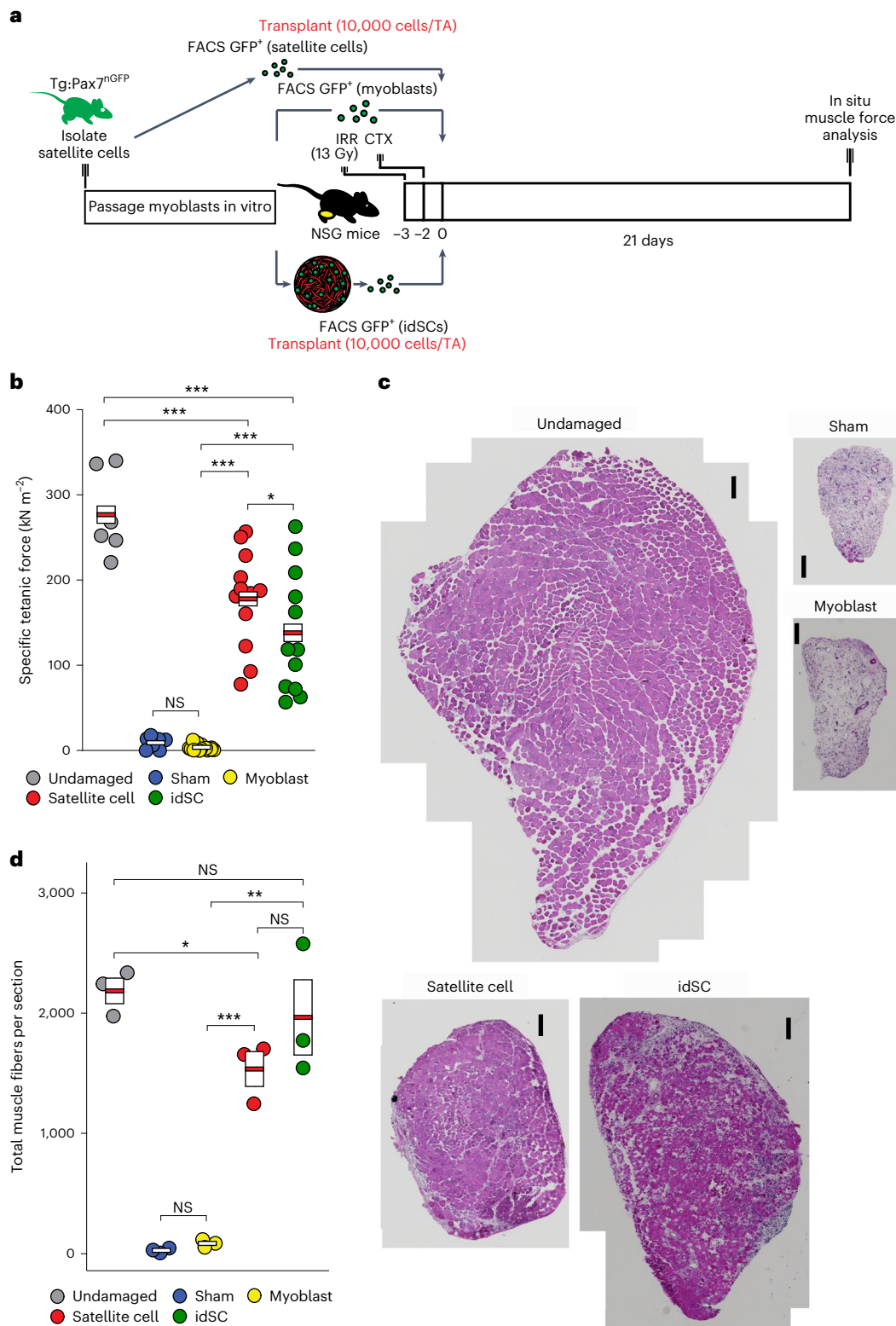
Fig. 6 | idSCs are similar to satellite cells in their capacity to generate functional muscle after transplantation into regenerating muscle.
a, Experimental schematic outlining the transplant of 10,000 nGFP+ cells (myoblasts, idSCs or freshly isolated satellite cells) into irradiated (IRR) and subsequently damaged TA muscles of NSG mice. **b**, Specific maximum tetanic force assessed on TA muscles 21 d after CTX damage. Undamaged muscle and sham transplants gave rise to specific force values of 278 ± 20.24 kN $\times$ m^{-2} and 8 ± 2.47 kN $\times$ m^{-2}, respectively. Box bounds represent s.e.m.; red line represents mean ($n = 6$ undamaged, $n = 8$ sham, $n = 15$ Myo, $n = 12$ SC, $n = 12$ idSC, biological replicates). Student's two-tailed t-test, unpaired with equal variance assumed and no multiple testing correction between samples. P values: undamaged

versus idSC 2.56×10^{-7}; undamaged versus SC 9.02×10^{-5}; Myo versus idSC 1.37×10^{-9}; Myo versus SC 6.88×10^{-13}; SC versus idSC 0.0405; Myo versus sham 0.818; *$P < 0.05$, ***$P < 0.001$. **c**, Stitched hematoxylin and eosin micrographs of cross-sectioned TA muscle 21 d after cell transplant. Scale bars, 100 μm.
d, Total muscle fibers per section across samples. Box bounds represent s.e.m.; red line represents mean ($n = 3$, biological replicates). Student's two-tailed t-test, unpaired with equal variance assumed and no multiple testing correction between samples. P values: undamaged versus idSC 0.358; undamaged versus SC 0.0175; Myo versus idSC 9.22×10^{-6}; SC versus idSC 0.0897; Myo versus SC 8.39×10^{-5}; Myo versus sham 0.804; *$P < 0.05$, **$P < 0.01$, ***$P < 0.001$. NS, not significant; SC, satellite cell.

muscle force generation to primary satellite cells (Supplementary Fig. 8). Our approach, although not fully optimized, meets the criteria of a satellite cell as detailed above.

The physical properties and extracellular signals of the stem cell niche facilitate the maintenance of satellite cell function[50,64,66,68,84–89]. We observed enrichment of type V collagens in both the epigenomic and transcriptional signatures shared by late-stage idSCs and satellite cells (Figs. 2a and 3d). Type V collagens were previously demonstrated as being important components of the quiescent satellite cell niche and specific downstream targets of Notch signaling[44]. Furthermore, our epigenomic and transcriptional analysis of idSCs identified an increase in the expression of key ECM components present in the satellite cell niche[43,45,66,90–93] and genes associated with functional regulation of muscle regeneration[42,44] (Figs. 2a,c,d and 3c,d and Supplementary Figs. 3b–d and 4c,d). Together, these data suggest that SkMOs contain a niche similar to that found in vivo such that idSCs can appear, survive and expand.

Our results support the hypothesis that 3D culture is permissive for several processes that cause myoblasts to dedifferentiate into idSCs and maintain them in a satellite cell-like state. First, as idSCs appear during organoid growth, large-scale epigenomic remodeling occurs, resulting in the progressive silencing of the myogenic program (Fig. 3a–c and Supplementary Fig. 4d)[23,94–96]. In parallel and likely, as a consequence, myoblast-specific E-box sites transition to an unbound state on their target promoters during idSC maturation to eventually match satellite cells (Fig. 3c–f). These temporal changes in the epigenetic state during dedifferentiation culminate in late-stage idSCs having a satellite cell-like epigenomic profile, including proteins associated with the satellite cell state and Notch pathway members (Fig. 3c,d and Supplementary Fig. 4d). Likewise, at the transcriptional level, these same genes are modulated in idSCs as they are in satellite cells (Fig. 2a,c,d and Supplementary Fig. 3b,c).

Our data suggest that myoblasts first lose their identity at the epigenomic level before activation of core satellite cell transcriptional pathways (Notch, ECM and quiescence biomarkers) during idSC maturation. In addition, freshly isolated idSCs demonstrate the rapid induction of genes associated with satellite cell activation[43,45,97,98], including *MAPK/AP-1*, *Egr* family members and *PI3K/Akt* modulation (Fig. 2 and Supplementary Figs. 3b,d and 4c,e). Alongside these epigenomic and transcriptional changes, idSCs show hallmarks of the endogenous satellite cell's quiescent state, including a lack of DNA replication (Fig. 1e,f), downregulated cell cycle genes (Fig. 2c,d), reduced cell size (Fig. 1g,h), absence of MyoD protein (Fig. 1c,d) and upregulation of the quiescence factors *Spry1* and *Wnt4* (Fig. 2a,c and Supplementary Fig. 3b)[4,99]. Mouse idSCs, when compared to adult human satellite cells[100–102] or engineered adult human skeletal muscle[103], display key conserved satellite cell signatures (ECM, Notch pathway, downregulation of MyoD and cell cycle-related genes), demonstrating significant similarities across species, further supporting the feasibility to efficiently produce human idSCs when starting from muscle biopsies.

These findings demonstrate that idSCs are similar to satellite cells with respect to their functional capacity in vivo, despite differences both at the transcriptional (Fig. 2d, Supplementary Fig. 3d and Supplementary Table 3) and epigenomic (Fig. 3a and Supplementary Fig. 4c) levels. Thus, our findings suggest core changes, as outlined above, that must occur in myoblasts to facilitate their dedifferentiation in vitro. Whether idSCs acquire these functional properties in vitro, or are sufficiently primed to gain them once placed in a damaged environment in vivo, remains to be determined. To date, when studying quiescent adult satellite cells, the field is limited to approximately 100,000 FACS-sorted cells per mouse. It is now feasible using our organoid method to readily generate 3 million idSCs per spinner flask (Supplementary Fig. 1d), using common and inexpensive equipment. Perturbing the pathways involved during idSC formation may offer the ability to leverage previously identified small-molecule[64,65],

biologic[68,89] and ECM[44,50,104] modulators to improve this process. Thus, given the time required for their formation, the abundance of idSCs generated, the possibility to store them frozen and the potential for purification using cell surface markers, the SkMO system may facilitate studies into how myogenic cells dedifferentiate and regain satellite cell function.

To produce human idSC equivalents, we tested clinically relevant modifications, including producing SkMOs from human myoblasts in serum-free medium and in a shortened timeline (Supplementary Fig. 9a). We determined that, after 15 d in culture, human SkMOs contain PAX7+ cells that have returned to a quiescent state and do not express MYOD, both hallmarks of human satellite cells (Supplementary Fig. 9c–h). Analysis of canonical human myogenic cell surface markers, used to compare human myoblasts to cells from dissociated SkMOs, did not readily identify candidates for purification (Supplementary Fig. 9b). To these ends, future approaches to identifying cell surface markers for the purification of human idSCs/SCs from myoblasts could include CyTOF[28], single-cell proteomics[105] or screening commercial cell surface libraries[106]. Additionally, single-cell transcriptomics from a timecourse of human SkMO generation would further inform how to translate this method from mouse to human.

One hurdle in clinical cell therapy is producing cells at scale[107]. Our current method (spinner flask culture or orbital shake culture) should be readily transferable to methods used for mid-scale and large-scale production of allogeneic cells[107,108]. However, autologous use of our cells would require less expansion/batch yet would demand the ability to generate cells across a series of patients. Currently, even before optimization, we successfully generated thousands of SkMOs/batch across four patient myoblast samples, some even highly passaged. A human TA muscle is approximately 1,000 times the weight of a mouse TA muscle. Currently, we can regenerate all of the damaged muscle of a mouse TA devoid of its own satellite cells after the transplant of 10,000 idSCs into an irradiated and CTX-treated NSG mouse (Fig. 6d). With further optimization of our manufacturing protocol and culture medium[109], our data suggest that we will be able to produce 10 million human idSCs from a single muscle biopsy. That should be sufficient to repair a human TA muscle. From a translational perspective, this may be a viable approach to generate autologous cells to treat patients with genetic disorders that affect a subset of muscles, trauma-induced muscle damage (sports, accident or military related) and age-related muscle weakness (sarcopenia). Future iterations of our method, in combination with gene therapy or CRISPR-mediated gene editing, could maintain muscle mass and deliver corrected genes targeted toward a variety of degenerative genetic muscle disorders.

Online content

Any methods, additional references, Nature Portfolio reporting summaries, source data, extended data, supplementary information, acknowledgements, peer review information; details of author contributions and competing interests; and statements of data and code availability are available at https://doi.org/10.1038/s41587-024-02344-7.

References

1. Mauro, A. Satellite cell of skeletal muscle fibers. *J. Biophys. Biochem Cytol*. **9**, 493–495 (1961).
2. Sambasivan, R. et al. Pax7-expressing satellite cells are indispensable for adult skeletal muscle regeneration. *Development* **138**, 3647–3656 (2011).
3. Brack, A. S. & Rando, T. A. Intrinsic changes and extrinsic influences of myogenic stem cell function during aging. *Stem Cell Rev*. **3**, 226–237 (2007).
4. Shea, K. L. et al. Sprouty1 regulates reversible quiescence of a self-renewing adult muscle stem cell pool during regeneration. *Cell Stem Cell* **6**, 117–129 (2010).

5. Chakkalakal, J. V., Jones, K. M., Basson, M. A. & Brack, A. S. The aged niche disrupts muscle stem cell quiescence. *Nature* **490**, 355–360 (2012).

6. Kuang, S., Kuroda, K., Le Grand, F. & Rudnicki, M. A. Asymmetric self-renewal and commitment of satellite stem cells in muscle. *Cell* **129**, 999–1010 (2007).

7. Collins, C. A. et al. Stem cell function, self-renewal, and behavioral heterogeneity of cells from the adult muscle satellite cell niche. *Cell* **122**, 289–301 (2005).

8. Yin, H., Price, F. & Rudnicki, M. A. Satellite cells and the muscle stem cell niche. *Physiol. Rev.* **93**, 23–67 (2013).

9. Lepper, C., Partridge, T. A. & Fan, C. M. An absolute requirement for Pax7-positive satellite cells in acute injury-induced skeletal muscle regeneration. *Development* **138**, 3639–3646 (2011).

10. Beauchamp, J. R., Morgan, J. E., Pagel, C. N. & Partridge, T. A. Dynamics of myoblast transplantation reveal a discrete minority of precursors with stem cell-like properties as the myogenic source. *J. Cell Biol.* **144**, 1113–1122 (1999).

11. Almada, A. E. & Wagers, A. J. Molecular circuitry of stem cell fate in skeletal muscle regeneration, ageing and disease. *Nat. Rev. Mol. Cell Biol.* **17**, 267–279 (2016).

12. Montarras, D. et al. Direct isolation of satellite cells for skeletal muscle regeneration. *Science* **309**, 2064–2067 (2005).

13. Sherwood, R. I. et al. Isolation of adult mouse myogenic progenitors: functional heterogeneity of cells within and engrafting skeletal muscle. *Cell* **119**, 543–554 (2004).

14. Sacco, A., Doyonnas, R., Kraft, P., Vitorovic, S. & Blau, H. M. Self-renewal and expansion of single transplanted muscle stem cells. *Nature* **456**, 502–506 (2008).

15. Barker, N. et al. Lgr5^{+ve} stem cells drive self-renewal in the stomach and build long-lived gastric units in vitro. *Cell Stem Cell* **6**, 25–36 (2010).

16. Huch, M. et al. Long-term culture of genome-stable bipotent stem cells from adult human liver. *Cell* **160**, 299–312 (2015).

17. Rigamonti, A. et al. Large-scale production of mature neurons from human pluripotent stem cells in a three-dimensional suspension culture system. *Stem Cell Rep.* **6**, 993–1008 (2016).

18. Quarta, M. et al. An artificial niche preserves the quiescence of muscle stem cells and enhances their therapeutic efficacy. *Nat. Biotechnol.* **17**, 267–279 (2016).

19. Sharir, A. et al. A large pool of actively cycling progenitors orchestrates self-renewal and injury repair of an ectodermal appendage. *Nat. Cell Biol.* **21**, 1102–1112 (2019).

20. Loomans, C. J. M. et al. Expansion of adult human pancreatic tissue yields organoids harboring progenitor cells with endocrine differentiation potential. *Stem Cell Rep.* **10**, 712–724 (2018).

21. Hu, H. et al. Long-term expansion of functional mouse and human hepatocytes as 3D organoids. *Cell* **175**, 1591–1606 (2018).

22. Seale, P. et al. Pax7 is required for the specification of myogenic satellite cells. *Cell* **102**, 777–786 (2000).

23. Rudnicki, M. A. et al. MyoD or Myf-5 is required for the formation of skeletal muscle. *Cell* **75**, 1351–1359 (1993).

24. Megeney, L. A., Kablar, B., Garrett, K., Anderson, J. E. & Rudnicki, M. A. MyoD is required for myogenic stem cell function in adult skeletal muscle. *Genes Dev.* **10**, 1173–1183 (1996).

25. Lancaster, M. A. & Knoblich, J. A. Organogenesis in a dish: modeling development and disease using organoid technologies. *Science* **345**, 1247125 (2014).

26. Ingwall, J. S., Morales, M. F. & Stockdale, F. E. Creatine and the control of myosin synthesis in differentiating skeletal muscle. *Proc. Natl Acad. Sci. USA* **69**, 2250–2253 (1972).

27. Sambasivan, R. et al. Distinct regulatory cascades govern extraocular and pharyngeal arch muscle progenitor cell fates. *Dev. Cell* **16**, 810–821 (2009).

28. Porpiglia, E. et al. High-resolution myogenic lineage mapping by single-cell mass cytometry. *Nat. Cell Biol.* **19**, 558–567 (2017).

29. Rodgers, J. T. et al. mTORC1 controls the adaptive transition of quiescent stem cells from G_0 to G_{Alert}. *Nature* **510**, 393–396 (2014).

30. Rodgers, J. T., Schroeder, M. D., Ma, C. & Rando, T. A. HGFA is an injury-regulated systemic factor that induces the transition of stem cells into G_{Alert}. *Cell Rep.* **19**, 479–486 (2017).

31. Sato, T. et al. Single Lgr5 stem cells build crypt-villus structures in vitro without a mesenchymal niche. *Nature* **459**, 262–265 (2009).

32. Maritan, S. M., Lian, E. Y. & Mulligan, L. M. An efficient and flexible cell aggregation method for 3D spheroid production. *J. Vis. Exp.* 55544 (2017).

33. Abe-Fukasawa, N., Otsuka, K., Aihara, A., Itasaki, N. & Nishino, T. Novel 3D liquid cell culture method for anchorage-independent cell growth, cell imaging and automated drug screening. *Sci. Rep.* **8**, 3627 (2018).

34. Watt, F. M. & Jensen, K. B. Epidermal stem cell diversity and quiescence. *EMBO Mol. Med.* **1**, 260–267 (2009).

35. Yoshida, N., Yoshida, S., Koishi, K., Masuda, K. & Nabeshima, Y. Cell heterogeneity upon myogenic differentiation: down-regulation of MyoD and Myf-5 generates 'reserve cells'. *J. Cell Sci.* **111**, 769–779 (1998).

36. Abou-Khalil, R., Le Grand, F. & Chazaud, B. Human and murine skeletal muscle reserve cells. *Methods Mol. Biol.* **1035**, 165–177 (2013).

37. Burton, A. & Torres-Padilla, M. E. Chromatin dynamics in the regulation of cell fate allocation during early embryogenesis. *Nat. Rev. Mol. Cell Biol.* **15**, 723–734 (2014).

38. Ma, S. et al. Chromatin potential identified by shared single-cell profiling of RNA and chromatin. *Cell* **183**, 1103–1116 (2020).

39. Corces, M. R. et al. An improved ATAC-seq protocol reduces background and enables interrogation of frozen tissues. *Nat. Methods* **14**, 959–962 (2017).

40. Stark, R. & Brown, G. DiffBind: differential binding analysis of ChIP-Seq peak data. http://bioconductor.org/packages/release/bioc/vignettes/DiffBind/inst/doc/DiffBind.pdf (Bioconductor, 2011).

41. McLean, C. Y. et al. GREAT improves functional interpretation of *cis*-regulatory regions. *Nat. Biotechnol.* **28**, 495–501 (2010).

42. Dumont, N. A. et al. Dystrophin expression in muscle stem cells regulates their polarity and asymmetric division. *Nat. Med.* **21**, 1455–1463 (2015).

43. Machado, L. et al. In situ fixation redefines quiescence and early activation of skeletal muscle stem cells. *Cell Rep.* **21**, 1982–1993 (2017).

44. Baghdadi, M. B. et al. Reciprocal signalling by Notch–Collagen V–CALCR retains muscle stem cells in their niche. *Nature* **557**, 714–718 (2018).

45. van Velthoven, C. T. J., de Morree, A., Egner, I. M., Brett, J. O. & Rando, T. A. Transcriptional profiling of quiescent muscle stem cells in vivo. *Cell Rep.* **21**, 1994–2004 (2017).

46. Bentsen, M. et al. ATAC-seq footprinting unravels kinetics of transcription factor binding during zygotic genome activation. *Nat. Commun.* **11**, 4267 (2020).

47. Thorne, N., Inglese, J. & Auld, D. S. Illuminating insights into firefly luciferase and other bioluminescent reporters used in chemical biology. *Chem. Biol.* **17**, 646–657 (2010).

48. Shaner, N. C. et al. Improved monomeric red, orange and yellow fluorescent proteins derived from *Discosoma* sp. red fluorescent protein. *Nat. Biotechnol.* **22**, 1567–1572 (2004).

49. Shultz, L. D. et al. Human lymphoid and myeloid cell development in NOD/LtSz-*scid IL2Rγ^{null}* mice engrafted with mobilized human hemopoietic stem cells. *J. Immunol.* **174**, 6477–6489 (2005).

50. Gilbert, P. M. et al. Substrate elasticity regulates skeletal muscle stem cell self-renewal in culture. *Science* **329**, 1078–1081 (2010).

51. Chapman, V. M., Miller, D. R., Armstrong, D. & Caskey, C. T. Recovery of induced mutations for X chromosome-linked muscular dystrophy in mice. *Proc. Natl Acad. Sci. USA* **86**, 1292–1296 (1989).

52. Boldrin, L., Neal, A., Zammit, P. S., Muntoni, F. & Morgan, J. E. Donor satellite cell engraftment is significantly augmented when the host niche is preserved and endogenous satellite cells are incapacitated. *Stem Cells* **30**, 1971–1984 (2012).

53. Parent, V. A., Tremblay, J. P. & Garnier, A. Rational design of a serum-free culture medium for the growth of human myoblasts destined to cell therapy. *Can. J. Chem. Eng.* **94**, 1855–1862 (2016).

54. Gussoni, E. et al. Normal dystrophin transcripts detected in Duchenne muscular dystrophy patients after myoblast transplantation. *Nature* **356**, 435–438 (1992).

55. Huard, J. et al. Human myoblast transplantation: preliminary results of 4 cases. *Muscle Nerve* **15**, 550–560 (1992).

56. Karpati, G. et al. Myoblast transfer in Duchenne muscular dystrophy. *Ann. Neurol.* **34**, 8–17 (1993).

57. Mendell, J. R. et al. Myoblast transfer in the treatment of Duchenne's muscular dystrophy. *N. Engl. J. Med.* **333**, 832–838 (1995).

58. Law, P. K. et al. Dystrophin production induced by myoblast transfer therapy in Duchenne muscular dystrophy. *Lancet* **336**, 114–115 (1990).

59. Perie, S. et al. Autologous myoblast transplantation for oculopharyngeal muscular dystrophy: a phase I/IIa clinical study. *Mol. Ther.* **22**, 219–225 (2014).

60. Peters, K. M. et al. Autologous muscle derived cells for treatment of stress urinary incontinence in women. *J. Urol.* **192**, 469–476 (2014).

61. Boyer, O. et al. Autologous myoblasts for the treatment of fecal incontinence: results of a phase 2 randomized placebo-controlled study (MIAS). *Ann. Surg.* **267**, 443–450 (2018).

62. Fu, X. et al. Combination of inflammation-related cytokines promotes long-term muscle stem cell expansion. *Cell Res.* **25**, 655–673 (2015).

63. Ding, S. et al. Maintaining bovine satellite cells stemness through p38 pathway. *Sci. Rep.* **8**, 10808 (2018).

64. Cosgrove, B. D. et al. Rejuvenation of the muscle stem cell population restores strength to injured aged muscles. *Nat. Med.* **20**, 255–264 (2014).

65. Buchanan, S. M. et al. Pro-myogenic small molecules revealed by a chemical screen on primary muscle stem cells. *Skelet. Muscle* **10**, 28 (2020).

66. Price, F. D. et al. Inhibition of JAK-STAT signaling stimulates adult satellite cell function. *Nat. Med.* **20**, 1174–1181 (2014).

67. Judson, R. N. et al. Inhibition of methyltransferase Setd7 allows the in vitro expansion of myogenic stem cells with improved therapeutic potential. *Cell Stem Cell* **22**, 177–190 (2018).

68. Ho, A. T. V. et al. Prostaglandin E2 is essential for efficacious skeletal muscle stem-cell function, augmenting regeneration and strength. *Proc. Natl Acad. Sci. USA* **114**, 6675–6684 (2017).

69. Mashinchian, O. et al. An engineered multicellular stem cell niche for the 3D derivation of human myogenic progenitors from iPSCs. *EMBO J.* **41**, e110655 (2022).

70. Afshar Bakooshli, M. et al. A 3D culture model of innervated human skeletal muscle enables studies of the adult neuromuscular junction. *eLife* **8**, e44530 (2019).

71. Faustino Martins, J. M. et al. Self-organizing 3D human trunk neuromuscular organoids. *Cell Stem Cell* **26**, 172–186 (2020).

72. Chal, J. et al. Differentiation of pluripotent stem cells to muscle fiber to model Duchenne muscular dystrophy. *Nat. Biotechnol.* **33**, 962–969 (2015).

73. Choi, I. Y. et al. Concordant but varied phenotypes among Duchenne muscular dystrophy patient-specific myoblasts derived using a human iPSC-based model. *Cell Rep.* **15**, 2301–2312 (2016).

74. Caron, L. et al. A human pluripotent stem cell model of facioscapulohumeral muscular dystrophy-affected skeletal muscles. *Stem Cells Transl. Med.* **5**, 1145–1161 (2016).

75. Xu, C. et al. A zebrafish embryo culture system defines factors that promote vertebrate myogenesis across species. *Cell* **155**, 909–921 (2013).

76. Xi, H. et al. A human skeletal muscle atlas identifies the trajectories of stem and progenitor cells across development and from human pluripotent stem cells. *Cell Stem Cell* **27**, 158–176 (2020).

77. Sasai, Y. Next-generation regenerative medicine: organogenesis from stem cells in 3D culture. *Cell Stem Cell* **12**, 520–530 (2013).

78. Arsic, N., Mamaeva, D., Lamb, N. J. & Fernandez, A. Muscle-derived stem cells isolated as non-adherent population give rise to cardiac, skeletal muscle and neural lineages. *Exp. Cell. Res.* **314**, 1266–1280 (2008).

79. Sarig, R., Baruchi, Z., Fuchs, O., Nudel, U. & Yaffe, D. Regeneration and transdifferentiation potential of muscle-derived stem cells propagated as myospheres. *Stem Cells* **24**, 1769–1778 (2006).

80. Westerman, K. A. Myospheres are composed of two cell types: one that is myogenic and a second that is mesenchymal. *PLoS ONE* **10**, e0116956 (2015).

81. Juhas, M. & Bursac, N. Roles of adherent myogenic cells and dynamic culture in engineered muscle function and maintenance of satellite cells. *Biomaterials* **35**, 9438–9446 (2014).

82. Tiburcy, M. et al. Regeneration competent satellite cell niches in rat engineered skeletal muscle. *FASEB Bioadv.* **1**, 731–746 (2019).

83. Cerletti, M. et al. Highly efficient, functional engraftment of skeletal muscle stem cells in dystrophic muscles. *Cell* **134**, 37–47 (2008).

84. Madl, C. M., Heilshorn, S. C. & Blau, H. M. Bioengineering strategies to accelerate stem cell therapeutics. *Nature* **557**, 335–342 (2018).

85. Jones, N. C. et al. The p38α/β MAPK functions as a molecular switch to activate the quiescent satellite cell. *J. Cell Biol.* **169**, 105–116 (2005).

86. Bernet, J. D. et al. p38 MAPK signaling underlies a cell-autonomous loss of stem cell self-renewal in skeletal muscle of aged mice. *Nat. Med.* **20**, 265–271 (2014).

87. Tierney, M. T. et al. STAT3 signaling controls satellite cell expansion and skeletal muscle repair. *Nat. Med.* **20**, 1182–1186 (2014).

88. Le Grand, F., Jones, A. E., Seale, V., Scime, A. & Rudnicki, M. A. Wnt7a activates the planar cell polarity pathway to drive the symmetric expansion of satellite stem cells. *Cell Stem Cell* **4**, 535–547 (2009).

89. Sampath, S. C. et al. Induction of muscle stem cell quiescence by the secreted niche factor Oncostatin M. *Nat. Commun.* **9**, 1531 (2018).

90. Bentzinger, C. F. et al. Fibronectin regulates Wnt7a signaling and satellite cell expansion. *Cell Stem Cell* **12**, 75–87 (2013).

91. Fukada, S. et al. Molecular signature of quiescent satellite cells in adult skeletal muscle. *Stem Cells* **25**, 2448–2459 (2007).

92. Pallafacchina, G. et al. An adult tissue-specific stem cell in its niche: a gene profiling analysis of in vivo quiescent and activated muscle satellite cells. *Stem Cell Res.* **4**, 77–91 (2010).

93. De Micheli, A. J. et al. Single-cell analysis of the muscle stem cell hierarchy identifies heterotypic communication signals involved in skeletal muscle regeneration. *Cell Rep.* **30**, 3583–3595 (2020).

94. Soleimani, V. D. et al. Snail regulates MyoD binding-site occupancy to direct enhancer switching and differentiation-specific transcription in myogenesis. *Mol. Cell* **47**, 457–468 (2012).

95. Asakura, A., Komaki, M. & Rudnicki, M. Muscle satellite cells are multipotential stem cells that exhibit myogenic, osteogenic, and adipogenic differentiation. *Differentiation* **68**, 245–253 (2001).

96. Asakura, A. et al. Increased survival of muscle stem cells lacking the *MyoD* gene after transplantation into regenerating skeletal muscle. *Proc. Natl Acad. Sci. USA* **104**, 16552–16557 (2007).

97. van den Brink, S. C. et al. Single-cell sequencing reveals dissociation-induced gene expression in tissue subpopulations. *Nat. Methods* **14**, 935–936 (2017).

98. Kimmel, J. C., Hwang, A. B., Scaramozza, A., Marshall, W. F. & Brack, A. S. Aging induces aberrant state transition kinetics in murine muscle stem cells. *Development* **147**, dev183855 (2020).

99. Eliazer, S. et al. Wnt4 from the niche controls the mechano-properties and quiescent state of muscle stem cells. *Cell Stem Cell* **25**, 654–665 (2019).

100. De Micheli, A. J., Spector, J. A., Elemento, O. & Cosgrove, B. D. A reference single-cell transcriptomic atlas of human skeletal muscle tissue reveals bifurcated muscle stem cell populations. *Skelet. Muscle* **10**, 19 (2020).

101. Rubenstein, A. B. et al. Single-cell transcriptional profiles in human skeletal muscle. *Sci. Rep.* **10**, 229 (2020).

102. Lovric, A. et al. Single-cell sequencing deconvolutes cellular responses to exercise in human skeletal muscle. *Commun. Biol.* **5**, 1121 (2022).

103. Wang, J. et al. Myoblast deactivation within engineered human skeletal muscle creates a transcriptionally heterogeneous population of quiescent satellite-like cells. *Biomaterials* **284**, 121508 (2022).

104. Ishii, K. et al. Recapitulation of extracellular LAMININ environment maintains stemness of satellite cells in vitro. *Stem Cell Rep.* **10**, 568–582 (2018).

105. Single-cell proteomics: challenges and prospects. *Nat. Methods* **20**, 317–318 (2023).

106. Uezumi, A. et al. Cell-surface protein profiling identifies distinctive markers of progenitor cells in human skeletal muscle. *Stem Cell Rep.* **7**, 263–278 (2016).

107. Lee, B. et al. Cell culture process scale-up challenges for commercial-scale manufacturing of allogeneic pluripotent stem cell products. *Bioeng. (Basel)* **9**, 92 (2022).

108. Costariol, E. et al. Demonstrating the manufacture of human CAR-T cells in an automated stirred-tank bioreactor. *Biotechnol. J.* **15**, e2000177 (2020).

109. Gotti, E. et al. Optimization of therapeutic T cell expansion in G-Rex device and applicability to large-scale production for clinical use. *Cytotherapy* **24**, 334–343 (2022).

Publisher's note Springer Nature remains neutral with regard to jurisdictional claims in published maps and institutional affiliations.

¹Department of Stem Cell and Regenerative Biology, Harvard University, Cambridge, MA, USA. ²Harvard Stem Cell Institute, Harvard University, Cambridge, MA, USA. ³Stanley Center for Psychiatric Research, Broad Institute of MIT and Harvard, Cambridge, MA, USA. ⁴Department of Systems Biology and Laboratory of Systems Pharmacology, Harvard Medical School, Boston, MA, USA. ⁵Department of Organismic and Evolutionary Biology, Harvard University, Cambridge, MA, USA. ⁶Division of Genetics and Genomics and the Stem Cell Program, Boston Children's Hospital, Boston, MA, USA. ✉e-mail: feodor_price@harvard.edu; lee_rubin@harvard.edu

Methods

Animals
We used the following mouse lines: C57BL/6J (Jax no. 000664), *Tg:Pax7^{nGFP}* mice (provided by Shahragim Tajbakhsh, Institut Pasteur), *mdx5cv Rag* null (provided by E.G.) and NOD.CG-*Prkdc*^{scid}IL2rg^{tm1Wjl}/SzJ (NSG) (Jax no. 005557). All mice were housed in a 12:12 hour light–dark cycle at 21–25 °C and 30%–75% humidity with ad libitum access to food and water. All experiments were approved by and performed in accordance with Harvard University Institutional Animal Care and Use Committee guidelines for animal handling and care. A mixture of male and female mice was used to obtain satellite cells and derive myoblasts lines. All NSG mice used in this study were male.

Cell culture
"Satellite cells" refers to cells freshly isolated by FACS and immediately used, whereas "primary myoblasts" refers to cells derived from satellite cells, cultured in vitro for longer than two weeks, and used for experiments between passage 5 and 15. Satellite cells and primary myoblast lines were derived using hindlimb skeletal muscle from C57BL/6J, *Tg:Pax7^{nGFP}* mice as previously described[24,27]. Briefly, hindlimb skeletal muscles were aseptically dissected from either male or female 2- to 6-month-old mice, minced, and digested in a dispase and collagenase solution (1 mg ml⁻¹ collagenase and 4 mg ml⁻¹ dispase II, Roche) for 10 min (triturated after 5 min) at 37 °C. The slurry was pelleted at 543*g* for 5 min and subsequently filtered through a 100-μm cell strainer (Corning). Cells were washed in FACS buffer several times before FACS sorting or culture in vitro. For the derivation of primary myoblast lines, cells were cultured in growth medium: Ham's F10 (Wisent), 20% heat inactivated FBS (Sigma Aldrich), 5 ng ml⁻¹ human bFGF, Aldevron), non-essential amino acids and Glutamax (Gibco) on collagen-coated plates (rat tail collagen) (Corning), at 37 °C with 5% CO₂. Following culture ex vivo for 1 week, myoblasts were purified on the basis of nGFP (*Tg:Pax7^{nGFP}*) or α7 integrin (UBC Ablab). Purified myoblasts were passaged five times before being frozen as cell stocks. Differentiated myotubes or reserve cells were generated from proliferative myoblasts, grown to confluence, and subsequently cultured for 5 days in differentiation medium: DMEM (Gibco), 5% heat inactivated horse serum (Life Technologies), non-essential amino acids and Glutamax (Gibco) on laminin-coated plates (Thermo Fisher Scientific). Human myoblasts were either purchased from a commercial vendor (Gibco, unknown passage) or provided by E.G. (passage 8). Human myoblasts were expanded and further enriched for expression of the CD82 cell surface marker and subsequently frozen as stocks (passage 10–15). Myoblasts were thawed and expanded on collagen-coated dishes in growth medium: Ham's F10 (Wisent), 20% FBS (Sigma Aldrich), 10 ng ml⁻¹ human bFGF (Aldevron), non-essential amino acids and Glutamax (Gibco).

Skeletal muscle organoid formation
Mouse skeletal muscle organoids (SkMOs) were generated from myoblasts (passage 5–15) cultured in growth medium on collagen coated plates. Myoblasts were expanded on ten 15-cm plates (Westnet) before adaptation to 3D culture. Optimal seeding densities and spin rates were determined empirically and were based on a previous publication from the lab[17]. One million myoblasts per milliliter (50 million cells per spinner flask) were seeded into a 125-ml spinner flask (Corning) on a nine-position stir plate (Dura-Mag) at 55 r.p.m. in a 37 °C incubator with 5% CO₂. Cells were seeded in spin medium: DMEM:F12 (Gibco), 20% heat inactivated FBS (Sigma Aldrich), 10 ng ml⁻¹ human bFGF (Aldevron), non-essential amino acids and Glutamax (Gibco). SkMOs were fed every 48 h by allowing the organoids to settle, aspirating medium and adding 50 ml of fresh spin medium. After 20 days, the medium was changed to differentiation medium for 10 days. Human SkMO formation was conducted using human myoblasts seeded into Elplasia plates (Corning) at 10,000 myoblasts per microcavity in human serum-free medium: Ham's F10:RPMI1640, non-essential amino acids,

Glutamax, B27, insulin transferrin selenium (ITS), lipid concentrate (all from Thermo Fisher Scientific), 500 μg ml⁻¹ BSA, 1 μM dexamethasone (Sigma Aldrich), 10 ng ml⁻¹ EGF (Biolegend), 10 ng ml⁻¹ human bFGF (Aldeveron) and 1 μM Repsox (Selleckchem). Preformed human SkMOs received four medium changes over a period of 48 h before being transferred to 10-cm ULA plates (Corning). Human SkMOs were maintained in human serum-free medium for 8 days on an orbital shaker (IKA) at 100 r.p.m. and transferred to human differentiation medium (DMEM, non-essential amino acids, Glutamax (all from Gibco)) for 5 days with shaking. Harvard Institutional Review Board approval was awarded to conduct work with human samples in this study.

Lentiviral production and infection
Third-generation lentivirus was produced in 293T cells using the following plasmids: for the expression vector pCDH-EF1-Luc2-P2A-tdTomato (a gift from Kazuhiro Oka; Addgene no. 72486) was produced in combination with packaging plasmids pMDLg (Addgene plasmid no. 12251), pRSV-Rev (Addgene plasmid no. 12253) and pMD2.G (Addgene plasmid no. 12259)[110]. Myoblasts were infected with lentivirus to express luciferase and tdTomato (LT) in the presence of polybrene (Sigma) at a concentration of 5 μg ml⁻¹ overnight. Myoblast lines were subsequently enriched for tdTomato-positive cells by FACS.

Flow cytometry and FACS analysis
SkMOs were rinsed with PBS and digested in a 50-ml falcon tube with collagenase/dispase solution at a final concentration of 1 mg ml⁻¹ DNase I (Worthington). Following trituration, the cell suspension was quenched with FBS and pelleted. Dissociated SkMO cells, satellite cells from hindlimb skeletal muscle, primary myoblasts or reserve cells were resuspended in FACS buffer and filtered through a 50-μm filter (Partec) before FACS sorting. Cells were separated on a MoFlo cytometer (Dako-Cytomation) on the basis of their expression of nGFP or staining with commercially available antibodies (Supplementary Table 6). Cells were incubated with conjugated antibodies for 30 min and filtered through a 50-μm filter (Partec) before analysis. Sorted satellite cells were either used immediately for experiments or expanded in culture as myoblast lines before SkMO generation. Flow cytometry scatter plots were generated and analyzed using FlowJo v10.0.

Cell size experiments
Following purification based on nGFP expression, cells were placed onto a microscope slide with FACS buffer and covered with a coverslip. Cells were imaged immediately without fixation using phase contrast on a Nikon Eclipse Ti. Cell diameter was determined using the Photoshop measurement tool.

Clonal spheroid experiments
Satellite cells, idSCs or myoblasts were sorted into a 96-well spheroid microplate (Corning) directly from the Astrios or MoFlo sorter (Beckman Coulter) and incubated at 37 °C. The percentage of wells containing a single cell was assessed after 24 h. For the clonal assay, cells were allowed to grow in spin medium for 10 days and given 100 μl of fresh medium on day 5. Cells were counted using a manual counter.

Immunofluorescence staining and microscopy
Muscle tissues were dissected and fixed with 0.5% PFA (Electron Microscopy Sciences) for 1 h, washed with PBS (Corning) several times and incubated overnight in 30% sucrose (Sigma Aldrich), all at 4 °C. SkMOs were processed in an identical fashion. Tissues were embedded in O.C.T./sucrose (2:1, Tissue-Tek) and frozen. Sections were cut (12–15 μm) and stored at −80 °C until use. Cultured cells were fixed in 0.5% PFA (Electron Microscopy Sciences) for 5 min and subsequently rinsed with PBS (Corning) before storage at 4 °C. Before antibody staining, samples were incubated at room temperature for 30 min in blocking solution (2% BSA (VWR), 5% goat serum (Life Technologies), 0.2% Triton

X-100 (Sigma Aldrich) and 0.02% sodium azide (Sigma Aldrich)). Muscle sections were preblocked in M.O.M. blocking buffer (Vector Laboratories) for 30 min at room temperature before being incubated with blocking solution. Primary antibodies (Supplementary Table 5) were diluted in blocking solution and incubated at room temperature for 1 h. Samples were then rinsed with PBS and incubated with secondary antibodies at room temperature in the dark. Samples were rinsed with PBS and counterstained with Hoechst, mounted (Dako Fluorescence Mounting Medium), coverslipped and imaged. To label proliferating cells, 5-ethynyl-2′-deoxyuridine (EdU, Lumiprobe) was administered subcutaneously (50 mg per kg body weight) or added directly to culture medium (1 μM) followed by a 48-h chase period. Visualization of signal was conducted using a ClickiT EdU cell proliferation kit (Life Technologies) according to the manufacturer's instructions followed by immunofluorescence staining. All samples were imaged on either a Nikon Eclipse TE2000-S or a Nikon Eclipse Ti unless otherwise specified.

Engraftment, repopulation and self-renewal experiments

Cell transplant into tibialis anterior (TA) muscle was conducted as described previously[66]. Briefly, bilateral TA muscle damage was created in adult 2- to 6-month-old male NSG mice following an intramuscular injection using an insulin syringe containing 50 μl of 10 μM CTX (Millipore-Sigma). Consistent levels of damage were observed to exceed 80% of the TA muscle. Parental myoblast lines derived from *Tg:Pax7^nGFP* mice and infected with LT lentivirus were used to generate idSCs. Either myoblasts or idSCs were FACS purified and immediately transplanted (10,000 nGFP⁺ tdTomato⁺ cells per TA) 48 h after CTX injection. All engraftment, repopulation, self-renewal and muscle force experiments were blinded. Bioluminescence imaging (BLI) was conducted on anesthetized (2% isoflurane, MWI Veterinary Supply) mice injected subcutaneously with D-luciferin (Gold Biotechnology) at a concentration of 150 mg kg⁻¹ body weight. BLI was performed using an IVIS-Spectrum (Perkin Elmer) at the plateau phase of D-luciferin perfusion, approximately 15 min after subcutaneous injection. Data analysis was conducted using Living-Image Software (Xenogen) to determine the average radiance present in a manually created region of interest conserved across all experiments and background subtracted. For *Rag*-null *mdxScv* engraftment and repopulation experiments, the hindlimbs of 6- to 12-week-old mice were irradiated at 13 Gy (X-Rad, Precision X-ray) 1 day before transplantation, in which 10,000 freshly sorted nGFP⁺ satellite cells, idSCs or myoblasts were injected into non-CTX-damaged TA muscle. One cohort of mice was collected for histology before re-injury at day 21 while the remaining mice were collected for histology at day 42.

In situ muscle function experiments

The hindlimb muscles of NSG mice were irradiated at 13 Gy (X-Rad, Precision X-ray) 3 days before cell transplant. Mice were anesthetized with a xylazine/ketamine cocktail (100 mg kg⁻¹ ketamine, 15 mg kg⁻¹ xylazine) during hindlimb irradiation. Myoblasts, idSCs, and satellite cells were FACS purified and immediately transplanted (10,000 nGFP⁺ cells per TA) 48 h after injection of 50 μl of 10 μM CTX. Undamaged controls were irradiated while sham controls were irradiated and injected with 50 μl of saline. For in situ muscle force experiments, mice were anesthetized (2% isoflurane) and placed ventrally on a 37 °C heated stage, and the leg was dissected to expose the TA. The fascia was removed, and a suture (Monocryl monofilament, Ethicon) was tied around the tendon of the TA muscle using a double surgeon's knot before the tendon was severed. Muscle force experiments were conducted on a 1300-A whole mouse test system (Aurora Scientific). The sutured distal tendon was affixed to the motor lever and positioned perpendicular to the TA muscle. Both electrodes were placed along the belly of the TA, with the cathode closest to the peroneal nerve. Calibrated Dynamic Muscle Control and Analysis software (Aurora Scientific) and a 701C bi-phase stimulator (Aurora Scientific) were used to acquire muscle

force measurements. Following stimulation and data collection, the optimal muscle length was calculated using calipers measuring from the patellar tendon to the TA distal tendon where the knot was tied. TA muscles were subsequently dissected, weighed, fixed in 0.5% PFA for 1 h, washed with PBS and incubated overnight in 30% sucrose at 4 °C. Sections were cut (12–15 μm), stained with hematoxylin and eosin, and imaged on a Zeiss AxioScan.

Transcriptional profiling

RNA for qPCR analysis was extracted using an RNEasy Mini kit (Qiagen) and 500 ng–1 μg of total RNA was reverse transcribed using the iScript kit (Bio-Rad) according to the manufacturer's instructions. qPCR was conducted using Fast SYBR Green reagents (Life Technologies) targeting specific genes (Supplementary Table 6) on a QuantStudio 12k Flex Real-Time PCR system (Applied Biosystems). Primer quality was assessed on the basis of the presence of a single melt curve peak. The fold change in gene expression was determined based on the $2^{-\Delta\Delta CT}$ method[111]. Statistical significance of qPCR values was based on comparison between dCT values[112]. For RNA-seq, RNA was extracted using a Total RNA Purification Plus kit (Norgen Biotek) and quantified using a Nanodrop (Thermo Fisher Scientific). 50 ng of total RNA in 10 μL of water was mixed with 10 μL of 1× TCL lysis buffer with 1% (vol/vol) β-mercaptoethanol (Qiagen). Each sample was added to triplicate wells in 384-well plates, which were stored at −80 °C. Before library construction, the plate was thawed, vortexed, and centrifuged for 1 min at 188*g*. 28 μL of SPRI beads (Beckman Coulter Genomics) were added directly to the sample, mixed and incubated for 5 min. The plate was transferred to a magnetic rack to aggregate the beads and incubated for 5 min before removing the supernatant. The beads were washed with 80% ethanol and dried for 1 min. 20 μL of nuclease-free water was added per well, the plate was removed from the magnetic rack, and the beads were thoroughly resuspended. Following a 5-min incubation, the plate was returned to the magnetic rack and incubated for an additional 5 min before transferring the supernatant to a fresh PCR plate. 5 μL of the supernatant was transferred to a separate plate containing RT master mix and 3′ and 5′ adapters for reverse transcription and template switching and incubated for 90 min at 42 °C (ref. 113). The cDNA was pooled and purified with a QIAquick PCR purification kit (Qiagen) according to the manufacturer's directions with a final elution in 24 μL of nuclease-free water, followed by an exonuclease I treatment for 30 min at 37 °C that was stopped with a 20-min incubation at 80 °C. The cDNA was then amplified using the Advantage 2 PCR Enzyme System (Takara) for 5 cycles and purified using AMPure XP magnetic beads (Beckman Coulter Genomics). Library preparation was completed with 55 ng input using a Nextera DNA kit (Illumina) following the manufacturer's instructions. The library was amplified 5 cycles and purified with AMPure XP magnetic beads (Beckman Coulter Genomics). A Pippin PREP purification of the sample from 300 to 800 bp was performed, quantified by qPCR, and sequenced on a single Illumina NextSeq run with paired-end reads (17R1, 58R2) at the Harvard University Bauer Core Facility. Reads were de-multiplexed and aligned to mm10 via bwa aln -l 24 (ref. 113). Gene expression levels were determined by counting unique UMIs among reads with unambiguous gene mappings. The resulting expression matrix was further filtered by removing (1) samples with fewer than 3,000 genes detected, (2) RNA-associated genes (Mt_tRNA, Mt_rRNA, snoRNA, snRNA, misc_RNA, scaRNA, rRNA, sRNA), and (3) genes with fewer than 10 counts total that were seen in fewer than 4 samples. The R package edgeR 3.26.8 (R version 3.6.1) was used for differential expression analysis. KEGG pathway analysis was conducted using DAVID (https://david.ncifcrf.gov/).

Epigenomic profiling

ATAC-seq experiments were conducted according to the Omni-ATAC protocol[39]. Libraries were sequenced on an Illumina Nextseq 500 using 75-bp paired-end reads. Raw reads were trimmed of adapters using

NGmerge[114] and aligned to mm10 using Bowtie2 (ref. [115]). Mitochondrial reads were removed using removeChrom (https://github.com/jsh58/harvard) and PCR duplicates removed using Picard (http://broadinstitute.github.io/picard/). Aligned reads with low quality mapping scores were removed using SAMtools[116]. Alignment (bam) files were downsampled to a standard of ~200 M mapped reads using Picard. Peak calling was performed using Genrich (https://github.com/jsh58/Genrich). Bam files were sorted by name using SAMtools, and peaks were called using default ATAC parameters (-j -p 0.01 -a 200), excluding the ENCODE blacklist for mm10. Consensus peak sets from replicates were called using IDR (https://github.com/kundajelab/idr/). Differential peak accessibility and replicate concordance was performed using Diffbind[40] and ChromVAR[117] while functions of *cis*-regulatory regions were predicted using GREAT[41] and footprinting analysis was conducted using TOBIAS[46].

Quantification and statistical analysis
All results are presented as a mean ± s.e.m. Individual biological or technical replicates are shown when appropriate. Statistical analysis of two conditions used Student's two-tailed *t*-tests with equal variance and normality assumed, although not formally tested, with no multiple-testing correction unless otherwise specified. Paired *t*-tests were used for biologically matched samples and unpaired *t*-tests were used for unrelated samples.

Reporting summary
Further information on research design is available in the Nature Portfolio Reporting Summary linked to this article.

Data availability
The RNA sequencing data can be found on FigShare at https://doi.org/10.6084/m9.figshare.25917505. The GEO accession code for ATAC-seq data in this paper is GSE267952. No restrictions on data availability exist.

Code availability
Code is available upon request.

References
110. Dull, T. et al. A third-generation lentivirus vector with a conditional packaging system. *J. Virol.* **72**, 8463–8471 (1998).
111. Livak, K. J. & Schmittgen, T. D. Analysis of relative gene expression data using real-time quantitative PCR and the $2^{-\Delta\Delta C(T)}$ method. *Methods* **25**, 402–408 (2001).
112. Wilhelm, J. & Pingoud, A. Real-time polymerase chain reaction. *ChemBioChem* **4**, 1120–1128 (2003).
113. Soumillon, M., Cacchiarelli, D., Semrau, S., van Oudenaarden, A. & Mikkelsen, T. S. Characterization of directed differentiation by high-throughput single-cell RNA-seq. bioRxiv (2014).
114. Gaspar, J. M. NGmerge: merging paired-end reads via novel empirically-derived models of sequencing errors. *BMC Bioinf.* **19**, 536 (2018).
115. Langmead, B. & Salzberg, S. L. Fast gapped-read alignment with Bowtie 2. *Nat. Methods* **9**, 357–359 (2012).
116. Li, H. et al. The Sequence Alignment/Map format and SAMtools. *Bioinformatics* **25**, 2078–2079 (2009).
117. Schep, A. N., Wu, B., Buenrostro, J. D. & Greenleaf, W. J. chromVAR: inferring transcription-factor-associated accessibility from single-cell epigenomic data. *Nat. Methods* **14**, 975–978 (2017).

Author contributions
F.D.P. and M.N.M. designed and carried out experiments, analyzed results and wrote the manuscript. W.C., A.R.G., E.A.W. and R.M.G. designed and carried out experiments, analyzed results and edited the manuscript. S.A.B. designed and carried out experiments. K.M.H. and J.M.P. designed experiments, analyzed results and edited the manuscript. A.L., J.S., P.S., K.G. and I.T.P. carried out experiments and analyzed results. P.K.S. and M.S. edited the manuscript. K.L.P., E.G., S.M.B. and L.L.R. designed experiments, analyzed results and wrote the manuscript.

Competing interests
A patent is active in the United States (US11512291B2) based on this research. L.L.R. and F.D.P. are co-founders of Circle Therapeutics, Inc. Circle Therapeutics and National Resilience are both interested in developing therapeutics to treat skeletal muscle disorders. L.L.R. is a founder of Vesalius Therapeutics, a member of its scientific advisory board and a private equity shareholder. He is also on the advisory board of Alkahest, a Grifols company, which is focused on the plasma proteome, and is a scientific advisory board member of ProjenX and Corsalex. All are interested in formulating approaches intended to treat diseases of the nervous system and other tissues. With the exception of National Resilience, none of these companies provided any financial support for this work, and the current work is unrelated to work carried out at any of these companies. The remaining authors declare no competing interests.

Additional information
Supplementary information The online version contains supplementary material available at https://doi.org/10.1038/s41587-024-02344-7.

Correspondence and requests for materials should be addressed to Feodor D. Price or Lee L. Rubin.

Peer review information *Nature Biotechnology* thanks the anonymous reviewers for their contribution to the peer review of this work.

Reprints and permissions information is available at www.nature.com/reprints.

nature research

Corresponding author(s): Feodor Price, Lee Rubin

Last updated by author(s): May 29, 2024

Reporting Summary

Nature Research wishes to improve the reproducibility of the work that we publish. This form provides structure for consistency and transparency in reporting. For further information on Nature Research policies, see our Editorial Policies and the Editorial Policy Checklist.

Statistics

For all statistical analyses, confirm that the following items are present in the figure legend, table legend, main text, or Methods section.

n/a	Confirmed	
☐	☒	The exact sample size (*n*) for each experimental group/condition, given as a discrete number and unit of measurement
☐	☒	A statement on whether measurements were taken from distinct samples or whether the same sample was measured repeatedly
☐	☒	The statistical test(s) used AND whether they are one- or two-sided *Only common tests should be described solely by name; describe more complex techniques in the Methods section.*
☐	☒	A description of all covariates tested
☐	☒	A description of any assumptions or corrections, such as tests of normality and adjustment for multiple comparisons
☐	☒	A full description of the statistical parameters including central tendency (e.g. means) or other basic estimates (e.g. regression coefficient) AND variation (e.g. standard deviation) or associated estimates of uncertainty (e.g. confidence intervals)
☐	☒	For null hypothesis testing, the test statistic (e.g. *F*, *t*, *r*) with confidence intervals, effect sizes, degrees of freedom and *P* value noted *Give P values as exact values whenever suitable.*
☒	☐	For Bayesian analysis, information on the choice of priors and Markov chain Monte Carlo settings
☒	☐	For hierarchical and complex designs, identification of the appropriate level for tests and full reporting of outcomes
☒	☐	Estimates of effect sizes (e.g. Cohen's *d*, Pearson's *r*), indicating how they were calculated

Our web collection on statistics for biologists contains articles on many of the points above.

Software and code

Policy information about availability of computer code

Data collection	Dynamic Muscle Control and Analysis Software (Aurora Scientific)
Data analysis	R version 3.6.1, edgeR 3.26.8, DAVID (https://david.ncifcrf.gov/), Nmerge, Bowtie2, RemoveChrom, Picard, SamTools, IDR, Diffbind, ChromVAR, GREAT, TOBIAS, ClusterProfiler, msigdbr, Flojo v10.9

For manuscripts utilizing custom algorithms or software that are central to the research but not yet described in published literature, software must be made available to editors and reviewers. We strongly encourage code deposition in a community repository (e.g. GitHub). See the Nature Research guidelines for submitting code & software for further information.

Data

Policy information about availability of data

All manuscripts must include a data availability statement. This statement should provide the following information, where applicable:
- Accession codes, unique identifiers, or web links for publicly available datasets
- A list of figures that have associated raw data
- A description of any restrictions on data availability

The RNA sequencing data can be found on FigShare at https://doi.org/10.6084/m9.figshare.25917505. The GEO accession number for ATAC-seq data in this paper is GSE267952 and can be found at https://www.ncbi.nlm.nih.gov/geo/query/acc.cgi?acc=GSE267952. No restrictions on data availability exist.

Field-specific reporting

Please select the one below that is the best fit for your research. If you are not sure, read the appropriate sections before making your selection.

☒ Life sciences   ☐ Behavioural & social sciences   ☐ Ecological, evolutionary & environmental sciences

For a reference copy of the document with all sections, see nature.com/documents/nr-reporting-summary-flat.pdf

Life sciences study design

All studies must disclose on these points even when the disclosure is negative.

Sample size	No sample size calculation was performed. Sample sizes exceeded biological triplicate in all cases. Additional samples were conducted to provide a reasonable statistical conclusion balancing both time and budgetary constraints. Biological replicates are designated in the figures legends as n=# of replicates.
Data exclusions	For RNAseq data. The gene expression matrix was filtered by removing: (1) samples with fewer than 3000 genes detected; (2) RNA associated genes ("Mt_tRNA", "Mt_rRNA", "snoRNA", "snRNA", "misc_RNA", "scaRNA", "rRNA", "sRNA"); (3) genes with fewer than 10 counts total that are seen in less than 4 samples.
Replication	All attempts at replication were successful. Experiments were replicated at separate times by a variety of co-authors on the paper over the duration of the project.
Randomization	All mice were randomly organized into experimental groups. All samples were allocated into groups based on their cohort (myoblast, idSC, SC).
Blinding	Investigators were blinded for all experiments conducted in this paper with the exception being where a given cohort visually would be distinguishable (eg. Immunofluorescence experiments where the presence of an organoid would distinguish these samples from myoblast or intact muscle samples). All bioinformatic data was conduced in a blinded/unbiased manner. Engraftment, repopulation, self-renewal and muscle force experiments were all blinded for data collection and analysis.

Reporting for specific materials, systems and methods

We require information from authors about some types of materials, experimental systems and methods used in many studies. Here, indicate whether each material, system or method listed is relevant to your study. If you are not sure if a list item applies to your research, read the appropriate section before selecting a response.

Materials & experimental systems

n/a	Involved in the study
☐	☒ Antibodies
☐	☒ Eukaryotic cell lines
☒	☐ Palaeontology and archaeology
☐	☒ Animals and other organisms
☒	☐ Human research participants
☒	☐ Clinical data
☒	☐ Dual use research of concern

Methods

n/a	Involved in the study
☒	☐ ChIP-seq
☐	☒ Flow cytometry
☒	☐ MRI-based neuroimaging

Antibodies

Antibodies used	All antibodies are summarized in Table S6
Validation	Anti-Mouse Pax7 (Pax7) : https://dshb.biology.uiowa.edu/PAX7?quantity=1&keywords=pax7 Anti-Mouse MyoD (G-1) : https://www.scbt.com/p/myod-antibody-g-1 Anti-Mouse My HC (MF20) : https://dshb.biology.uiowa.edu/MF-20 Anti-Laminin : https://www.novusbio.com/products/laminin-antibody_nb300-144af647Ant Anti-GFP Rb : https://www.abcam.com/products/primary-antibodies/gfp-antibody-ab13970.html Anti- RFP : https://www.rockland.com/categories/primary-antibodies/rfp-antibody-pre-adsorbed-600-401-379/ Anti-Mouse Dystrophin : https://dshb.biology.uiowa.edu/MANDRA1-7A10 Anti-alpha7 Integrin : https://link.springer.com/protocol/10.1007/978-1-61779-343-1_3#Sec2 Anti-CD29 : https://www.thermofisher.com/antibody/product/CD29-Integrin-beta-1-Antibody-clone-eBioHMb1-1-HMb1-1-Monoclonal :/47-0291-82 Anti-Cxcr4 : https://www.biolegend.com/fr-ch/products/pe-anti-human-cd184-cxcr4-antibody-542 Anti-Cd34 : https://www.biolegend.com/fr-ch/products/apc-anti-human-cd34-antibody-6204 Anti-Vcam1 : https://www.biolegend.com/fr-ch/products/alexa-fluor-647-anti-mouse-cd106-antibody-3129

Anti-Notch3 : https://www.biolegend.com/fr-ch/products/alexa-fluor-647-anti-mouse-notch-3-antibody-5288
Anti-Cd339 : https://www.biolegend.com/fr-ch/products/pe-anti-mouse-cd339-jagged-1-antibody-8773
Anti-Sdc1 : https://www.biolegend.com/fr-ch/products/apc-anti-mouse-cd138-syndecan-1-antibody-7572
Anti-Cd140b : https://www.thermofisher.com/antibody/product/CD140b-PDGFRB-Antibody-clone-APB5-Monoclonal/17-1402-82
Anti-Cd9 : https://www.biolegend.com/fr-ch/products/alexa-fluor-647-anti-mouse-cd9-antibody-5566
Anti-Cd104 : https://www.biolegend.com/fr-ch/products/alexa-fluor-647-anti-mouse-cd104-antibody-9741
Anti-Cd44 : https://www.biolegend.com/fr-ch/products/alexa-fluor-647-anti-mouse-human-cd44-antibody-3098
Anti-Cd49e : https://www.biolegend.com/fr-ch/products/apc-anti-mouse-cd49e-antibody-16202
Anti-Cd200 : https://www.biolegend.com/fr-ch/products/apc-anti-mouse-cd200-ox2-antibody-7338
Anti-MYOD1 : https://www.thermofisher.com/antibody/product/MYOD-Antibody-clone-HL1372-Recombinant-Monoclonal/MA5-47019
Anti-CD44 : https://www.biolegend.com/fr-ch/products/brilliant-violet-421-anti-human-cd44-antibody-8801
Anti-CD49e : https://www.biolegend.com/fr-ch/products/pe-anti-human-cd49e-antibody-4102
Anti-CD104 : https://www.biolegend.com/fr-ch/products/pe-anti-human-cd104-antibody-4121
Anti-CD56 : https://www.biolegend.com/fr-ch/products/pe-cyanine7-anti-human-cd56-ncam-antibody-4584
Anti-CD184 : https://www.biolegend.com/fr-ch/products/apc-anti-human-cd184-cxcr4-antibody-539
Anti-THY1 : https://www.biolegend.com/fr-ch/products/pe-cyanine7-anti-human-cd90-thy1-antibody-8282
Anti-CD9 : https://www.biolegend.com/fr-ch/products/apc-anti-human-cd9-antibody-15072
Anti-SDC1 : https://www.biolegend.com/fr-ch/products/apc-anti-human-cd138-syndecan-1-antibody-7315
Anti-CD29 : https://www.biolegend.com/fr-ch/products/apc-anti-human-cd29-antibody-852
Anti-FGFR4 : https://www.biolegend.com/fr-ch/products/pe-anti-human-cd334-fgfr4-antibody-3763
Anti-KI67 : https://www.abcam.com/products/primary-antibodies/ki67-antibody-ab15580.html

Eukaryotic cell lines

Policy information about cell lines

Cell line source(s)	All mouse cell lines were primary lines derived in the lab from the mouse strains listed in the manuscript. 293T cells were purchased from ATCC. Gibco and Cook myoblast lines are commercially available. Human myoblast lines 1230, 1369 were provided by Dr. Emanuela Gussoni.
Authentication	Cell lines were authenticated based on their expression of myogenic surface markers/transcription factor and their phenotype to give rise to multinucleated myotubes in vitro or in vivo. 293T cells were not authenticated prior to being used to produce Lentivirus.
Mycoplasma contamination	All cell lines used in the manuscript tested negative for mycoplasma
Commonly misidentified lines (See ICLAC register)	No commonly misidentified lines were used in this study

Animals and other organisms

Policy information about studies involving animals; ARRIVE guidelines recommended for reporting animal research

Laboratory animals	Strain:mouse Lines:C57Bl/6, Tg:Pax7nGFP, mdx5cv, NSG Age:2-6months
Wild animals	No wild animals were used in this study
Field-collected samples	No field-collected samples were used in this study
Ethics oversight	Harvard IACUC protocol 26-17

Note that full information on the approval of the study protocol must also be provided in the manuscript.

Flow Cytometry

Plots

Confirm that:

☒ The axis labels state the marker and fluorochrome used (e.g. CD4-FITC).

☒ The axis scales are clearly visible. Include numbers along axes only for bottom left plot of group (a 'group' is an analysis of identical markers).

☒ All plots are contour plots with outliers or pseudocolor plots.

☒ A numerical value for number of cells or percentage (with statistics) is provided.

Methodology

Sample preparation	Briefly, hindlimb skeletal muscles were dissected from either male or female mice between the ages of 2-6 months. Muscles were aseptically dissected, minced and digested in a dispase and collagenase solution (1 mg/ml collagenase and 4 mg/ml dispase II, Roche) for 10 min (triturated briefly after 5 mins) at 37 °C. The digested muscle slurry was pelleted at 1700 rpm for 5 min (Heraeus Multifuge) and subsequently filtered through a 100μm cell strainer (Falcon). Cells were washed in FACS buffer

several times prior to FACS sorting or culture in vitro. SkMOs were rinsed with PBS and digested in a 50ml falcon tube with collagenase/dispase solution containing 1000u of DNAse (Worthington). Following trituration the cell suspension was quenched with FBS and pelleted. Dissociated SkMO cells, hindlimb skeletal muscle in the case of satellite cells, primary myoblasts or reserve cells were resuspended in FACS buffer and filtered through a 50um filter (Partec) prior to FACS sorting. Cells were separated on a MoFlo cytometer (DakoCytomation) based on their expression of nGFP. Sorted satellite cells were either used immediately for experiments, or expanded in culture as myoblast lines prior to SkMO generation.

Instrument	Moflo XDP or Astrios (DakoCytomation)
Software	FlowJo v10
Cell population abundance	FACS sorted cells were collected in 1.5ml eppendorf tubes. Pelleted at 6000rpm for 5min and resuspended in an appropriate volume of liquid for subsequent experiments. For transplantation, cells were resuspended in sterile saline (0.9% NaCl) at a concentration of 10,000 events/25ul prior to transplant. For RNAseq, cells were directly lysed for library construction according to the manufactures protocols. ATACseq experiments cells conducted according to the OMNI-ATAC protocol
Gating strategy	All FACS experiments initially involved gating the bulk population from debris based on SSC vs FSC followed by identification of singlets based on FSC height vs FSC weight. Indentification of GFP positive cells was conducted versus an empty PE channel to distinguish autofluorescence. A similar strategy was used to identify double positive GFP+ and TdTomato+ cells prior to transplant.

☒ Tick this box to confirm that a figure exemplifying the gating strategy is provided in the Supplementary Information.